Metadata of the article that will be visualized in OnlineFirst

ArticleTitle	Experimental study of high-Ti and low-Ti basalts: liquid lines of descent and silicate liquid immiscibility in large igneous provinces	
Article Sub-Title		
Article CopyRight	The Author(s), under exclusive licence to Springer-Verlag GmbH Germany, part of Springer Nature (This will be the copyright line in the final PDF)	
Journal Name	Contributions to Mineralogy and Petrology	
Corresponding Author	FamilyName	**Zhang**
	Particle	
	Given Name	**Yishen**
	Suffix	
	Division	Department of Earth and Environmental Sciences
	Organization	KU Leuven
	Address	3000, Leuven, Belgium
	Phone	
	Fax	
	Email	yishen.zhang@kuleuven.be
	URL	
	ORCID	http://orcid.org/0000-0002-4261-7565
Author	FamilyName	**Namur**
	Particle	
	Given Name	**Olivier**
	Suffix	
	Division	Department of Earth and Environmental Sciences
	Organization	KU Leuven
	Address	3000, Leuven, Belgium
	Phone	
	Fax	
	Email	
	URL	
	ORCID	
Author	FamilyName	**Charlier**
	Particle	
	Given Name	**Bernard**
	Suffix	
	Division	Department of Geology
	Organization	University of Liège
	Address	4000, Sart Tilman, Belgium
	Phone	
	Fax	
	Email	
	URL	
	ORCID	
Schedule	Received	8 Oct 2022
	Revised	
	Accepted	20 Dec 2022

Abstract	Dichotomous high-Ti and low-Ti magmas are ubiquitous in large igneous provinces (LIPs). These magmas often form economically critical Fe–Ti oxide ores in layered intrusions via mechanisms that remain debated. To constrain the evolution of high-Ti and low-Ti basalts during fractionation, we performed stepwise equilibrium crystallization experiments at atmospheric pressure. We specifically aimed to quantify the influences of starting composition and oxygen fugacity (fO_2) on phase stability, phase compositions, and the onset of silicate liquid immiscibility during cooling. Both types of magma crystallize similar phase assemblages at QFM (quartz–fayalite–magnetite thermodynamic equilibrium) and QFM + 2: olivine, clinopyroxene, plagioclase, Fe–Ti oxides, and whitlockite. Tridymite crystallizes late in experiments at QFM + 2. The starting composition exerts a strong influence on phase and melt compositions. High CaO and Al_2O_3 contents in the melt favor the early crystallization of plagioclase and enhance FeO enrichment before Fe–Ti oxide saturation. fO_2 affects the composition and stability of Fe–Ti oxides, and high fO_2 conditions may promote melt differentiation into the calc-alkaline field. Silicate liquid immiscibility occurs in both compositional trajectories, producing Fe-rich melt globules in equilibrium with Si-rich melts. Strong iron enrichment is not necessary for immiscibility to develop; unmixing also occurs in Fe depleted compositions. We propose a new parameterization to map the binodal surface in temperature-composition space that successfully fits the two-liquid field in experiments and natural immiscible compositions. Our results indicate that Fe–Ti oxide ores in layered intrusions associated with LIPs form by the segregation of Fe-rich melts and/or the accumulation of early crystallized Fe–Ti oxides during fractionation.
Keywords (separated by '-')	Flood basalt - Large igneous province - Immiscibility - Phase equilibria - Liquid line of descent
Footnote Information	Communicated by Othmar Müntener.The online version contains supplementary material available at https://doi.org/10.1007/s00410-022-01990-x.

Contributions to Mineralogy and Petrology _####################_
https://doi.org/10.1007/s00410-022-01990-x

ORIGINAL PAPER

Experimental study of high-Ti and low-Ti basalts: liquid lines of descent and silicate liquid immiscibility in large igneous provinces

Yishen Zhang[1] · **Olivier Namur**[1] · **Bernard Charlier**[2]

Received: 8 October 2022 / Accepted: 20 December 2022

Abstract

Dichotomous high-Ti and low-Ti magmas are ubiquitous in large igneous provinces (LIPs). These magmas often form economically critical Fe–Ti oxide ores in layered intrusions via mechanisms that remain debated. To constrain the evolution of high-Ti and low-Ti basalts during fractionation, we performed stepwise equilibrium crystallization experiments at atmospheric pressure. We specifically aimed to quantify the influences of starting composition and oxygen fugacity (fO_2) on phase stability, phase compositions, and the onset of silicate liquid immiscibility during cooling. Both types of magma crystallize similar phase assemblages at QFM (quartz–fayalite–magnetite thermodynamic equilibrium) and QFM + 2: olivine, clinopyroxene, plagioclase, Fe–Ti oxides, and whitlockite. Tridymite crystallizes late in experiments at QFM + 2. The starting composition exerts a strong influence on phase and melt compositions. High CaO and Al_2O_3 contents in the melt favor the early crystallization of plagioclase and enhance FeO enrichment before Fe–Ti oxide saturation. fO_2 affects the composition and stability of Fe–Ti oxides, and high fO_2 conditions may promote melt differentiation into the calc-alkaline field. Silicate liquid immiscibility occurs in both compositional trajectories, producing Fe-rich melt globules in equilibrium with Si-rich melts. Strong iron enrichment is not necessary for immiscibility to develop; unmixing also occurs in Fe depleted compositions. We propose a new parameterization to map the binodal surface in temperature-composition space that successfully fits the two-liquid field in experiments and natural immiscible compositions. Our results indicate that Fe–Ti oxide ores in layered intrusions associated with LIPs form by the segregation of Fe-rich melts and/or the accumulation of early crystallized Fe–Ti oxides during fractionation.

Keywords Flood basalt · Large igneous province · Immiscibility · Phase equilibria · Liquid line of descent

Introduction

Large igneous provinces (LIPs) are regions comprising extremely large volumes of mafic/ultramafic magmas erupted or emplaced in the upper crust within a relatively short time (~ 1–5 Myr; Bryan and Ernst 2008). As the largest volcanic episodes on Earth and occurred in both oceanic and continental crust, they are thought to result from hot mantle plumes causing high degrees of melting at the base of the lithosphere (Campbell and Griffiths 1990; Campbell 2005).

LIPs generally contain large volumes of moderately evolved, phenocryst-poor, lavas (< 8 wt% MgO) associated with rare picritic dikes, and, locally, ultramafic/mafic layered intrusions. They usually show a geochemical dichotomy between high-Ti and low-Ti compositions (Cox et al. 1967), which are discriminated based on their TiO_2 contents or ratios of Ti to highly incompatible trace elements (e.g., Ti/Y, Peate et al. 1992). These contrasting magma compositions may reflect lithologically distinct mantle sources and/or the degree to which the sources are enriched in incompatible elements (Marsh et al. 2001; Bryan and Ernst 2008; Ernst 2014; Heinonen et al. 2022). However, recent studies have scrutinized this classification, because the melt evolution during cooling, especially with respect to TiO_2, depends strongly on oxygen fugacity (fO_2), pressure, and temperature, and can produce a

---

Communicated by Othmar Müntener.

✉ Yishen Zhang
yishen.zhang@kuleuven.be

[1] Department of Earth and Environmental Sciences, KU Leuven, 3000 Leuven, Belgium

[2] Department of Geology, University of Liège, 4000 Sart Tilman, Belgium

continuum of lava compositions between high-Ti and low-Ti endmembers (e.g., Kamenetsky et al. 2012). In addition, differences between the $f\mathrm{O}_2$ conditions of high-Ti and low-Ti magmas, attributed to different degrees of crustal assimilation (e.g., Xu et al. 2003), influence phase equilibria, especially the crystallization of Fe–Ti oxides. Therefore, a low-Ti composition could theoretically evolve into a high-Ti composition if Fe–Ti oxide saturation is delayed (Hou et al. 2011).

To better understand the compositional diversity of LIPs, it is important to investigate the differentiation of high-Ti and low-Ti magmas and systematically evaluate the roles of primary magma composition and $f\mathrm{O}_2$ in determining phase relations and differentiation processes. Fe–Ti oxides ore deposits are commonly preserved in LIPs and are geochemically associated with high-Ti lavas (e.g., Pang et al. 2010; Zhang et al. 2018; Fan et al. 2013). The formation of these deposits remains controversial, they form by either the density-driven accumulation of Fe–Ti oxides during fractional crystallization (Charlier et al. 2010; Pang et al. 2008), or their crystallization from a segregated immiscible Fe-rich melt (Zhou et al. 2005, 2013; Fischer et al. 2016). However, tracking the onset of silicate immiscibility has relied heavily on relatively few experiments (e.g., Charlier and Grove 2012) and thermodynamic modelling (Ghiorso and Carmichael 1980; Ghiorso et al. 1983). Unfortunately, no valid predictive model for the development of immiscibility currently exists, hindering our ability to validate or invalidate whether of Fe–Ti oxide ore formation requires silicate liquid immiscibility.

In this study, we use a stepwise experimental approach to closely reproduce the fractional crystallization of high-Ti and low-Ti basalts under various $f\mathrm{O}_2$ conditions at atmospheric pressure. Our results show that the different starting compositions, i.e. primary magma variability, strongly affect phase and melt compositions. The early crystallization of plagioclase in the low-Ti composition may enhance FeO enrichment in the melt and crystallinity at a given degree of fractionation. Oxygen fugacity has a profound effect on the stability, saturation temperature and chemistry of Fe–Ti oxides, in turn affecting the differentiation of the melt with respect to FeO and MgO as well as other major elements. We demonstrate that the residual melts of high-Ti and low-Ti basalts at both low and high $f\mathrm{O}_2$ conditions develop silicate liquid immiscibility during cooling and fractionation. We propose a new parameterization to describe the binodal surface of the immiscible pairs and thus the temperature-composition space of the two-liquid field. We apply our model in the ~ 260 Ma Emeishan LIP, China, and show that the development of immiscibility in high-Ti lavas may contribute to the formation of Fe–Ti oxide ores.

Experimental strategy and analytical methods

Starting materials and experimental conditions

The high-Ti and low-Ti starting materials were selected based on a compiled database of lava compositions from the Emeishan LIP. Geochemical and structural features of the Emeishan province, such as kilometer-scale uplift, indicate its mantle plume origin (e.g., Chung and Jahn 1995; Xu et al. 2001). We consider the Emeishan province to be representative of world-wide LIPs; for example, they share similar bulk rock geochemistry with the Karoo LIP, Southern Africa (Fig. 1). Bulk-rock compositions of Emeishan rocks are classified as high-Ti and low-Ti using a threshold Ti/Y ratio of 500 (Xu et al. 2001; Xiao et al. 2004). Nonetheless, a continuum of bulk-rock Ti/Y ratios and TiO_2 contents are observed for both provinces (Fig. 1a, b). We excluded compositions with > 15 wt% MgO to avoid drastic bulk-rock compositional changes due to olivine ± spinel accumulation. Therefore, the bulk-rock compositions in our database should close to the true liquid compositions. Finally, we selected high-Ti and low-Ti experimental starting compositions (HT1 and LT1, respectively; Table 1) by averaging the major oxide compositions of each group at ~ 14 wt% MgO, corresponding to the estimated primary melt for the Emeishan LIP (Xu et al. 2020).

The starting materials for experiments are synthetic powders prepared from mixtures of high-purity oxides and silicates (SiO_2, TiO_2, Al_2O_3, MnO, MgO, Fe_2O_3, $CaSiO_3$, $AlPO_4$, Na_2SiO_3, $K_2Si_4O_9$, Cr_2O_3) in appropriate proportions. The $CaSiO_3$, Na_2SiO_3, and $K_2Si_4O_9$ silicates were produced by mixing appropriate proportions of carbonates and SiO_2, then reacted and decarbonated for 5 days at 1100 °C for $CaSiO_3$ and at 750 °C for Na_2SiO_3, and $K_2Si_4O_9$. The silicate compounds were then checked for homogeneity, no silica relics were observed. The products were weighed to ensure complete decarbonization and then grinded in ethanol in an agate mortar for 1 h.

We employed a three-step experimental approach to simulate fractional crystallization of the high-Ti and low-Ti starting compositions at $f\mathrm{O}_2$ conditions of QFM (quartz–fayalite–magnetite thermodynamic equilibrium) and QFM + 2 (Table 2). The corresponding $f\mathrm{O}_2$ conditions at different temperature were calculated following O'Neill (1987), and the obtained $f\mathrm{O}_2$ values are consistent with the estimated $f\mathrm{O}_2$ range of different LIPs (e.g., Bai et al. 2019; Freise et al. 2009; Cao and Wang 2022). Additional experiments, referring as 'step 4' in Table 1, were performed to explore the potential development of silicate liquid immiscibility at the lowest experimental temperature. In step 1 (runs ending in 's1' in Table 2), compositions

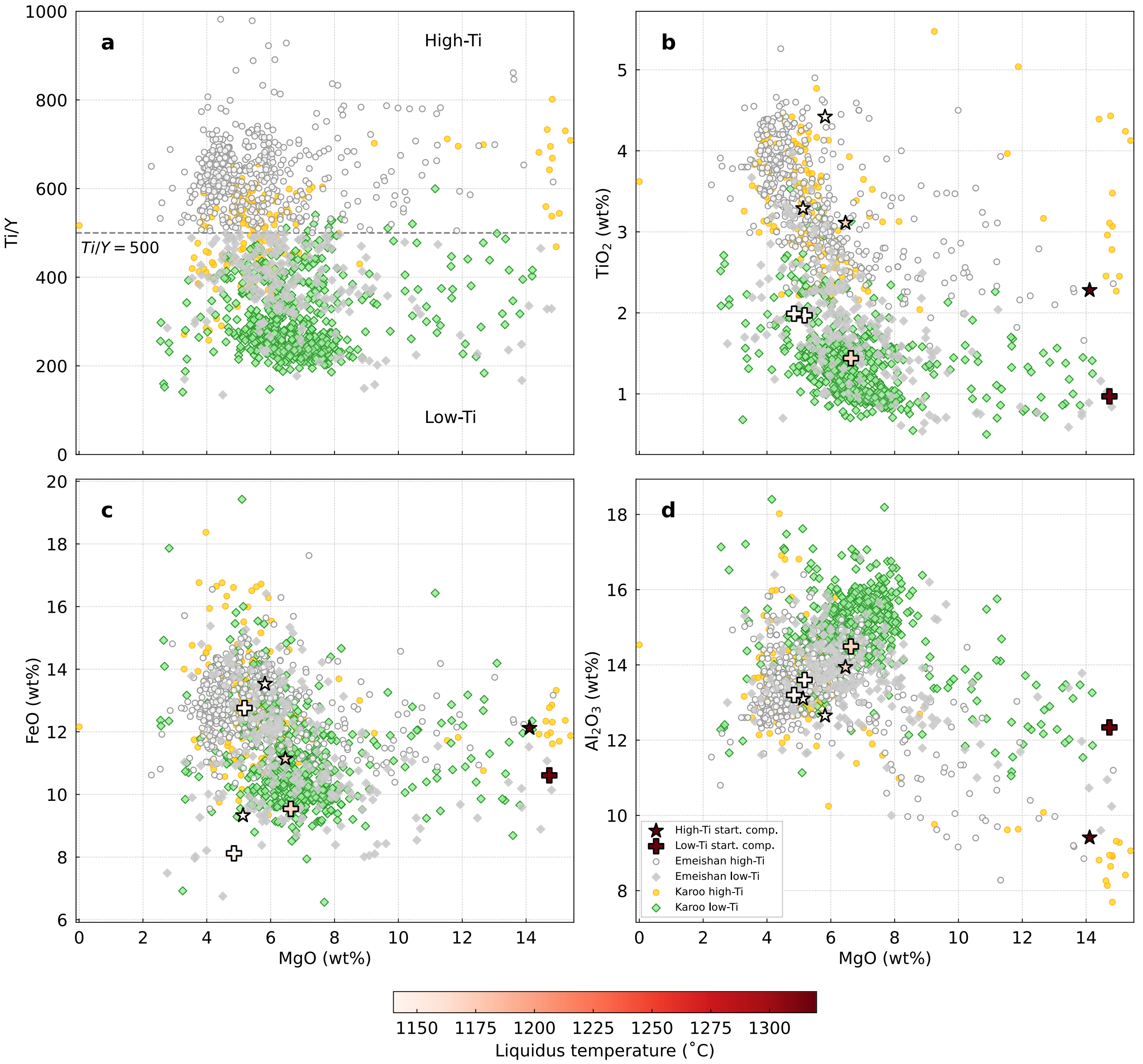

Fig. 1 Compositions of our starting materials compared to high-Ti and low-Ti lavas from the Emeishan and Karoo LIPs. The dashed line in **a** indicates Ti/Y = 500, the criterion used by Xu et al. (2001) to classify Emeishan lavas as high-Ti or low-Ti. Symbols indicating starting compositions according to their liquidus temperature. The Emeishan lavas are from a compiled database (Chung and Jahn 1995; Song et al. 2001; Xu et al. 2001; Xiao et al. 2004; Zhou et al. 2005, 2008; Zhang et al. 2006; Wang et al. 2007; Qi et al. 2008; Hanski et al. 2010; He et al. 2010; Kamenetsky et al. 2012; Tao et al. 2015; Arguin et al. 2016; Ren et al. 2017). Data for Karoo LIP are from the GEOROC database (https://georoc.mpch-mainz.gwdg.de//georoc/)

HT1 and LT1 were used for isothermal experiments at temperatures ranging from 1330 °C (super-liquidus) to 1160 °C. These compositions typically attained ~ 50% crystallinity at 1170 °C. Then, we prepared synthetic compositions HT2 and LT2 (Table 1) corresponding to the residual melts produced at 1170 °C under QFM + 2 in step 1 (runs 18As1 and 18Bs1). We prepared only these two new starting materials, because the compositions of the residual liquids at QFM are almost identical to those at QFM + 2 due to the absence of Fe–Ti oxide crystallization in the step 1 temperature interval (see below). These new compositions were used in step 2 (runs ending in ‘s2’in Table 2) for isothermal experiments at temperatures ranging from 1175 to 1120 °C. Due to the significant influence of fO_2 on the TiO$_2$ and FeO contents of the melts in this temperature range, particularly after saturation of

Table 1 Compositions (wt%) of starting materials in this and other studies

Sample no	SiO_2	TiO_2	Al_2O_3	FeOt	MnO	MgO	CaO	Na_2O	K_2O	P_2O_5	Cr_2O_3	Total	Ca#	Al#
This study														
HT1 (step 1)	48.79	2.28	9.41	12.12	0.18	14.11	10.74	2.03	0.51	0.20	0.13	100.12	0.84	0.16
HT2 (step 2)	49.91	3.11	13.93	11.14	0.16	6.46	12.37	2.55	0.42	0.22	0.02	100.29	0.83	0.22
HT31 (step 3 and 4)	48.43	4.42	12.65	13.53	0.19	5.82	10.40	2.13	0.81	0.23	0.02	98.63	0.83	0.21
HT32 (step 3 and 4)	54.63	3.29	13.10	9.33	0.21	5.13	9.19	2.82	0.83	0.19	0.04	98.76	0.77	0.19
LT1 (step 1)	49.09	0.97	12.34	10.61	0.17	14.73	11.31	1.32	0.76	0.10	0.14	99.54	0.90	0.20
LT2 (step 2)	53.68	1.44	14.49	9.54	0.19	6.63	11.91	1.96	0.95	0.16	0.02	99.97	0.86	0.21
LT31 (step 3 and 4)	53.89	1.97	13.60	12.76	0.17	5.18	9.42	1.43	1.19	0.18	0.01	99.80	0.87	0.20
LT32 (step 3 and 4)	59.90	1.99	13.20	8.12	0.19	4.85	8.00	1.67	1.58	0.16	0.01	99.67	0.83	0.18
Snyder et al. (1993)														
4-3	47.4	2.27	14.2	14.34	0.20	6.13	9.04	2.97	0.70	0.22	–	99.2	0.75	0.23
4-83C	46.2	3.83	13.4	17.33	0.22	4.66	7.58	3.56	1.03	0.35	–	99.5	0.68	0.22
Toplis and Carroll (1995)														
SC1	48.8	2.90	14.90	13.10	–	6.50	10.90	2.70	0.30	–	–	100.10	0.80	0.23

Ca# = Ca/(Na + Ca) and Al# = Al/(Al + Si)

Fe–Ti oxides, four starting materials with distinct FeO and TiO_2 contents were then synthesized as third-step compositions (HT31, LT31, HT32, and LT32; Table 1). These compositions correspond to the residual melt compositions produced at 1140 °C at QFM and QFM + 2 in step 2 (runs 11As2, 11Bs2, 12As2, and 12Bs2; Table 2). Step 3 experiments were performed with a 1 °C/h cooling rate from above the liquidus temperature (1160 °C) to final temperatures ranging from 1080 to 1040 °C.

An additional set of ten experiments (step 4) was performed with an identical cooling protocol and temperature range as step 3. Step 4 experiments were performed with the same four compositions as in step 3 but under different fO_2 conditions (see Table 2). For example, the high fO_2 starting materials (HT32 and LT32) of both series were used for additional experiments at more reduced conditions (QFM). This set of experiments was performed to test the development of liquid immiscibility in a variety of melt compositions under changing fO_2. The compositions of all starting materials are shown in Fig. 1.

Experimental methods

All experiments were performed in a GERO HTRV 70-250/18 vertical tube furnace at University of Liège, Belgium and in a Nabertherm HTRV 50/150/17 vertical tube furnace at KU Leuven, Belgium. Approximately 50 mg of the starting powders were suspended on a 0.2-mm-wide Pt loop and heated to a super-liquidus temperature for 10 min in a muffle furnace to produce glass. The starting glass was then suspended in the hot spot of the vertical furnace (~ 5 cm of the furnace where the temperature is within ± 1 °C). Experimental temperatures were measured using a S-type (Pt–$Pt_{90}Rh_{10}$) thermocouple calibrated against the melting points of Ag and Au. To minimize Fe loss from the starting materials, the Pt loops were pre-saturated in Fe by electroplating following the method of Grove (1981). Oxygen fugacity was buffered at QFM and QFM + 2 by flushing the furnace with mixtures of high-purity CO and CO_2 using Bronkhorst gas-flow controllers operating at a flow rate of 0.12 cm/s.

Isothermal experiments (steps 1 and 2) were equilibrated for 24–96 h at target temperatures between super-liquidus (1320–1330 °C) and 1120 °C. To produce crystals large enough for reliable analyses in lower temperature step 3 and step 4 experiments, we used a three-step approach: experiments were (1) held above the liquidus (1160 °C) for ~ 24 h, (2) cooled to 1080–1040 °C at a rate of 1 °C/h, and then (3) held at the final temperature for an additional 176–240 h. Four additional isothermal experiments (192 h durations) were performed at 1060 °C and QFM + 2 to compare their phase assemblages with the cooling experiments to check how the reliability of the cooling experiments and to verify whether the cooling experiments attained full thermodynamic equilibrium. All experiments were quenched by dropping the charges in water. Details on experimental conditions, run products, and phase proportions are reported in Table 2.

Analytical methods

The experimental charges were analyzed using a JEOL JXA-8530F wavelength dispersive spectrometer coupled to a field emission gun electron microprobe at University of Münster, Germany and at the Department of Material Engineering, KU Leuven, Belgium. We used a

Journal : Large 410 | Article No : 1990 | Pages : 25 | MS Code : 1990 | Dispatch : 2-1-2023

Table 2 Experimental conditions, phase assemblages, and phase proportions

Run no	Start. comp	T (°C)	Duration (h)	fO_2	Method	Phase assemblage	Phase proportions[a]	$\sum r^2$	ΔFe (%)	ΔNa (%)
Super-liquidus										
00A/00B	HT1/LT1	1330	24	QFM	Isothermal	Gl	–	–	–	–
22A/22B	HT1/LT1	1330	24	QFM + 2	Isothermal	Gl	–	–	–	–
2As2/10Bs2	HT2/LT2	1175	24	QFM	Isothermal	Gl	–	–	–	–
7As2/7Bs2	HT2/LT2	1175	24	QFM + 2	Isothermal	Gl	–	–	–	–
H104/H204/L104/L204	HT31/HT32 /LT31/LT32	1140	24	QFM + 2	Isothermal	Gl	–	–	–	–
Liquid lines of descent experiments (step 1–3)										
High-Ti experiments										
02As1	HT1	1320	24	QFM	Isothermal	Gl, Ol	98:02:00	0.47	0	2.36
01As1	HT1	1302	24	QFM	Isothermal	Gl, Ol	95:05:00	0.8	0	10.57
04As1	HT1	1280	48	QFM	Isothermal	Gl, Ol, Spl	92:07:01	0.17	0	11.51
03As1	HT1	1260	48	QFM	Isothermal	Gl, Ol, Spl	90:10:00	0.22	0	35.84
05As1	HT1	1240	48	QFM	Isothermal	Gl, Ol, Spl	88:12:00	0.31	0	8.02
06As1	HT1	1200	48	QFM	Isothermal	Gl, Ol, Spl, Aug	82:15:0:3	0.12	0	10.12
15As1	HT1	1180	72	QFM	Isothermal	Gl, Ol, Spl, Aug	74:16:0:10	0.24	0	7.45
17As1	HT1	1170	72	QFM	Isothermal	Gl, Ol, Spl, Aug	72:17:0:11	0.19	0.39	5.44
14As1	HT1	1160	72	QFM	Isothermal	Gl, Ol, Spl, Aug	67:17:0:16	0.05	0	9.89
1As2	HT2	1160	72	QFM	Isothermal	Gl, Aug, Pl	81:09:10	0.18	13.06	5.44
11As2	HT2	1140	72	QFM	Isothermal	Gl, Aug, Pl	61:20:19	0.06	1.1	0
3As2	HT2	1120	72	QFM	Isothermal	Gl, Aug, Pl, Mag	33:30:30:7	0.06	0	2.97
H105	HT31	1160–1080	176	QFM	1 °C/h	Gl, Aug, Pl, Ilm, Mag	36:30:25:4:5	0.44	0	1.31
H103	HT31	1160–1060	225	QFM	1 °C/h	Gl, Aug, Pl, Ilm, Mag, Wht (tr)	29:33:28:5:5:tr	0.05	0	7.61
H106	HT31	1160–1040	240	QFM	1 °C/h	Si-Gl, Fe-Gl, Aug, Pl, Ilm, Mag, Wht (tr)	26:0:34:28:6:6:tr	0.14	0	9.42
12As1	HT1	1320	24	QFM + 2	Isothermal	Gl	100	0	0	0
07As1	HT1	1302	24	QFM + 2	Isothermal	Gl, Ol	97:03:00	0.11	0	1.81
08As1	HT1	1280	48	QFM + 2	Isothermal	Gl, Ol, Spl	94:06:00	0.11	0	2.82
09As1	HT1	1260	48	QFM + 2	Isothermal	Gl, Ol, Spl	92:08:00	0.02	0	5.98
10As1	HT1	1240	48	QFM + 2	Isothermal	Gl, Ol, Spl	89:11:00	0.18	0	6.57
11As1	HT1	1200	48	QFM + 2	Isothermal	Gl, Ol, Spl	86:14:00	0.34	0	0
16As1	HT1	1180	72	QFM + 2	Isothermal	Gl, Ol, Spl, Aug	77:15:0:8	0.17	0	0
18As1	HT1	1170	72	QFM + 2	Isothermal	Gl, Ol, Spl, Aug	71:13:1:14	0.04	1.12	2.39
13As1	HT1	1160	72	QFM + 2	Isothermal	Gl, Ol, Spl, Aug	66:15:0:19	0.06	0	1.4
5As2	HT2	1160	72	QFM + 2	Isothermal	Gl, Aug, Pl, Mag	75:11:12:2	0.04	0	0
12As2	HT2	1140	72	QFM + 2	Isothermal	Gl, Aug, Pl, Mag, Psb	49:26:20:3:1	0.1	0	0
6As2	HT2	1120	96	QFM + 2	Isothermal	Gl, Aug, Pl, Mag (NA), Psb	–	–	–	–

Table 2 (continued)

Run no	Start. comp	T (°C)	Duration (h)	fO_2	Method	Phase assemblage	Phase proportions[a]	$\sum r^2$	ΔFe (%)	ΔNa (%)
H201	HT32	1160–1060	225	QFM + 2	1 °C/h	Gl, Aug, Pl, Mag, Psb, Wht (tr)	43:31:27:4:4:tr	0	0	0
H207	HT32	1160–1040	240	QFM + 2	1 °C/h	Si-Gl (NA), Fe-Gl (NA), Aug, Pl, Mag, Psb, Trd (tr), Wht (tr)	–	–	–	–
Low-Ti experiments										
02Bs1	LT1	1320	24	QFM	Isothermal	Gl, Ol	96:04:00	1.17	0	4.59
01Bs1	LT1	1302	24	QFM	isothermal	Gl, Ol	94:06:00	0.39	0	0
04Bs1	LT1	1280	48	QFM	Isothermal	Gl, Ol, Spl	92:08:00	0.49	0	0
03Bs1	LT1	1260	48	QFM	Isothermal	Gl, Ol, Spl	88:11:00	0.13	0.46	8.01
05Bs1	LT1	1240	48	QFM	Isothermal	Gl, Ol, Spl, Aug	86:14:0:0	0.25	0	0
06Bs1	LT1	1200	48	QFM	Isothermal	Gl, Ol, Spl, Aug	83:17:0:0	0.09	1.64	0
15Bs1	LT1	1180	72	QFM	Isothermal	Gl, Ol, Spl, Aug	74:17:0:9	0.93	0	0
17Bs1	LT1	1170	72	QFM	Isothermal	Gl, Ol, Aug, Pl	50:21:16:13	0.03	2.48	5.73
14Bs1	LT1	1160	72	QFM	Isothermal	Gl, Ol, Aug, Pl	42:21:19:18	0.03	1.89	0
8Bs2	LT2	1160	72	QFM	Isothermal	Gl, Aug, Pl	78:11:11	0.45	0	8.06
11Bs2	LT2	1140	72	QFM	Isothermal	Gl, Aug, Pl, Pig	65:18:18:0	1.56	0	0.48
9Bs2	LT2	1120	72	QFM	Isothermal	Gl (NA), Aug, Pl, Mag (NA), Pig	–	–	–	–
L105	LT31	1160–1080	176	QFM	1 °C/h	Gl, Aug, Pl, Mag	60:20:17:3	1.28	2.78	0
L103	LT31	1160–1060	225	QFM	1 °C/h	Gl, Aug, Pl, Mag, Pig, Wht (tr)	47:27:22:4:0:tr	0.22	0	5.7
L106	LT31	1160–1040	240	QFM	1 °C/h	Si-Gl, Fe-Gl, Aug, Pl, Mag, Wht (tr)	36:0:31:27:6:tr	0.9	0	3.99
12Bs1	LT1	1320	24	QFM + 2	Isothermal	Gl	100	3.59	0	4.39
07Bs1	LT1	1302	24	QFM + 2	Isothermal	Gl, Ol	99:01:00	0.92	0	0
08Bs1	LT1	1280	48	QFM + 2	Isothermal	Gl, Ol, Spl	96:04:00	0.39	0	0
09Bs1	LT1	1260	48	QFM + 2	Isothermal	Gl, Ol, Spl	94:06:00	0.22	0.9	0
10Bs1	LT1	1240	48	QFM + 2	Isothermal	Gl, Ol, Spl	91:09:00	0.23	0	0
11Bs1	LT1	1200	48	QFM + 2	Isothermal	Gl, Ol, Spl	87:12:00	0.09	0	0
16Bs1	LT1	1180	72	QFM + 2	Isothermal	Gl, Ol, Spl, Aug, Pl	69:13:0:13:5	0.11	0	0
18Bs1	LT1	1170	72	QFM + 2	Isothermal	Gl, Ol, Spl, Aug, Pl	44:14:0:24:17	0.07	9.09	0
13Bs1	LT1	1160	72	QFM + 2	Isothermal	Gl, Ol, Spl, Aug, Pl	33:14:1:29:23	0.06	6.39	4.77
5Bs2	LT2	1160	72	QFM + 2	Isothermal	Gl, Aug, Pl, Mag	70:15:14:1	0.01	0	1.56
12Bs2	LT2	1140	72	QFM + 2	Isothermal	Gl, Aug, Pl, Mag, Psb	51:26:21:2:0	0.27	0	0.18
6Bs2	LT2	1120	96	QFM + 2	Isothermal	Gl, Aug, Pl, Mag, Opx	36:31:29:4:0	0.5	0	2.11
L201	LT32	1160–1060	225	QFM + 2	1 °C/h	Gl, Aug, Pl, Mag, Trd (tr), Opx	56:21:18:5:tr:0	0.5	0	8.09
L207	LT32	1160–1040	240	QFM + 2	1 °C/h	Si-Gl (NA), Fe-Gl (NA), Aug, Pl, Mag, Trd (tr), Wht (tr)	–	–	–	–

Table 2 (continued)

Run no	Start. comp	T (°C)	Duration (h)	fO_2	Method	Phase assemblage	Phase proportions[a]	$\sum r^2$	ΔFe (%)	ΔNa (%)
Additional experiments for testing immiscibility (step 4)										
H205	HT32	1160–1080	176	QFM	1 °C/h	Gl, Aug, Pl, Ilm	59:21:20:1	1.64	0	20.4
H203	HT32	1160–1060	225	QFM	1 °C/h	Gl, Aug, Pl, Ilm, Mag, Opx, Wht (tr)	45:26:25:3:0:0:tr	0.92	0	20.56
H206	HT32	1160–1040	240	QFM	1 °C/h	Si-Gl, Fe-Gl, Aug, Pl, Ilm, Mag, Wht (tr)	35:0:32:28:5:0:tr	0.35	0	18.4
H101	HT31	1160–1060	225	QFM + 2	1 °C/h	Si-Gl, Fe-Gl (tr), Aug, Pl, Mag, Psb, Wht (tr)	27:tr:31:27:7:7:tr	0.05–	0.27	34.65
H107	HT31	1160–1040	240	QFM + 2	1 °C/h	Si-Gl (NA), Fe-Gl (NA), Aug, Pl, Mag, Psb, Trd (tr), Wht (tr)	–	–	–	–
L205	LT32	1160–1080	176	QFM	1 °C/h	Gl, Aug, Pl	87:13:00	5.55	0	7.37
L203	LT32	1160–1060	225	QFM	1 °C/h	Gl, Aug, Pl, Pig, Wht (tr)	66:18:16:0:tr	2.86	0	1.72
L206	LT32	1160–1040	240	QFM	1 °C/h	Si-Gl, Fe-Gl, Aug, Pl, Mag, Pig, Wht (tr)	55:0:24:20:2:tr	0.3	5.89	0
L101	LT31	1160–1060	225	QFM + 2	1 °C/h	Si-Gl, Fe-Gl (tr), Aug, Pl, Mag, Psb, Trd (tr)	42:tr:25:23:10:0:tr	0.28	0	24.25
L107	LT31	1160–1040	240	QFM + 2	1 °C/h	Si-Gl (NA), Fe-Gl (NA), Aug, Pl, Mag, Psb, Trd, Wht (tr)	–	–	–	–
Additional experiments for testing equilibrium										
H108	HT31	1060	192	QFM + 2	Isothermal	Gl (NA), Aug (NA), Pl (NA), Mag (NA)	–	–	–	–
H208	HT32	1060	192	QFM + 2	Isothermal	Gl (NA), Aug (NA), Pl (NA), Mag (NA)	–	–	–	–
L108	LT31	1060	192	QFM + 2	Isothermal	Gl (NA), Aug (NA), Pl (NA), Mag (NA)	–	–	–	–
L208	LT32	1060	192	QFM + 2	Isothermal	Gl (NA), Aug (NA), Pl (NA), Mag (NA), Psb (NA)	–	–	–	–

[a] NA indicates phases are too small to analysis. tr indicates trace amount

15 kV accelerating voltage and beam currents of 10 nA for glasses and 20 nA for minerals. Glasses were analyzed with a defocused beam (5–10 µm diameter) and minerals with a focused beam (~ 1 µm diameter). We measured Si, Ti, Al, Fe, Mn, Mg, Ca, Na, K, P, and Cr concentrations with on-peak and background counting times of 10 and 5 s, respectively. Na, Al, K, and Cr were analyzed first to minimize migration. Natural and synthetic primary standards (reported in the Appendix) were used, and the CITZAF online data correction package was used for matrix correction of all analyses (Armstrong 1995). To ensure accuracy and precision as well as consistency between analytical sessions, we measured the following secondary standards at regular intervals (every 80–100 points): VG-2 (NMNH 111240-52) for glass, San Carlos olivine (NMNH 111312-44) for olivine, kakanui augite for pyroxene (NMNH 122142), County Lake plagioclase (NMNH 115900) for plagioclase, ilmenite (NMNH 96189) for Fe–Ti oxides. Experimental phase compositions generally have ~ 98% accuracy for major elements. The complete dataset of glass and mineral analyses and primary and secondary standards is reported in the Appendix.

Attainment of equilibrium

In isothermal experiments (steps 1 and 2), we gauged the attainment of equilibrium mainly based on compositional and textural characteristics. Furthermore, the run durations presented herein are considerably longer than those in previous experimental studies (e.g., Toplis and Carroll 1995; Charlier and Grove 2012). Melts and minerals in experimental charges show homogeneous backscattered electron intensities (Fig. 2), except pyroxenes, which are known to show apparent sector zoning with prominent Al_2O_3 concentrations (Neave and Putirka 2017). Euhedral crystal morphologies indicate that equilibrium was attained. Fe–Mg partition coefficients between olivine and melt (K_D^{Fe-Mg} see Compositional details section) in our experiments are ~ 0.30 ± 0.02, in good agreement with previously reported values for similar compositions (0.30 ± 0.03; e.g., Toplis and Carroll 1995), further indicating that our experiments attained thermodynamic equilibrium.

To assess the degree of equilibrium attained in steps 3 and 4 cooling experiments, we compared those experiments with isothermal experiments performed at 1060 °C and QFM + 2. The cooling experiments produced larger crystals but had identical phase assemblages (melt, augite, plagioclase, and magnetite) as the isothermal experiments (Fig. S1). This confirms that our 1 °C/h cooling protocol did not hinder the attainment of equilibrium. Nevertheless, we report only the compositions of crystal rims in direct contact with melt.

Phase proportion estimates

Modal phase proportions were estimated using a non-negative least squares regression algorithm implemented using the SciPy module in Python (https://github.com/eazzzon/MassBalanceCal), in which we balanced the starting compositions with the average compositions of all analyzed phases in each experimental charge. The squared sum of the residuals ($\sum r^2$) was typically <0.5. A few experiments, mainly cooling experiments with zoned pyroxenes and/or zoned plagioclase resulted in $\sum r^2 > 1$. Fe loss (ΔFe) was calculated by adding a pure Fe phase in the mass balance calculation (Li et al. 2020). Our results show a maximum 13.1% Fe loss in only one run; minor to no Fe loss was detected in the rest of the experiments. We used a similar procedure to evaluate potential Na loss due to volatility in the atmosphere of the furnace (Tormey et al. 1987; Table 2). Calculated values were generally low (< 5–10%) but reached 35% in some low-temperature, near-solidus experiments. However, such Na loss estimations are strongly affected by the accuracy of microprobe Na analyse due to potential Na migration under the electron beam (Voigt et al. 2017), particularly in low-temperature experiments, where both residual melt pools and plagioclase crystals are small (< 2–3 µm) inhibiting analyses with large beam diameters. Such cases affect both least square calculations and measurement of elements in plagioclase. Consequently, Na losses reported in Table 2, AQ1 and especially the high values, should be taken with caution.

Experimental results

Phase equilibria and immiscibility textures

Figure 3 shows phase relations in the liquid lines of descent experiments (steps 1–3) and step 4 experiments as a function of temperature and fO_2 (QFM and QFM + 2). In both high-Ti and low-Ti liquid lines of descent experiments (steps 1–3), solid phases crystallizing upon cooling are olivine, Cr-spinel, augite, plagioclase, trace of low-Ca pyroxene (pigeonite and/or orthopyroxene), magnetite, ilmenite, pseudobrookite, whitlockite, and tridymite.

Olivine is the first liquidus phase in the primitive compositions HT1 and LT1 (1320–1160 °C). Cr-spinel joined the liquidus at around 1280–1260 °C, followed by the crystallization of augite at around 1240–1180 °C, and plagioclase at around 1180–1160 °C. These temperature ranges depend on both, the starting composition [low-Ti (LT1) vs high-Ti (HT1)] and fO_2 (QFM vs QFM + 2). Compared to experiments at QFM, olivine and augite saturation is delayed by ~ 20–40 °C at QFM + 2 in both high-Ti and low-Ti compositions. Plagioclase saturation is weakly dependent on fO_2 (1180 °C at QFM + 2 vs 1170 °C at QFM), but plagioclase in

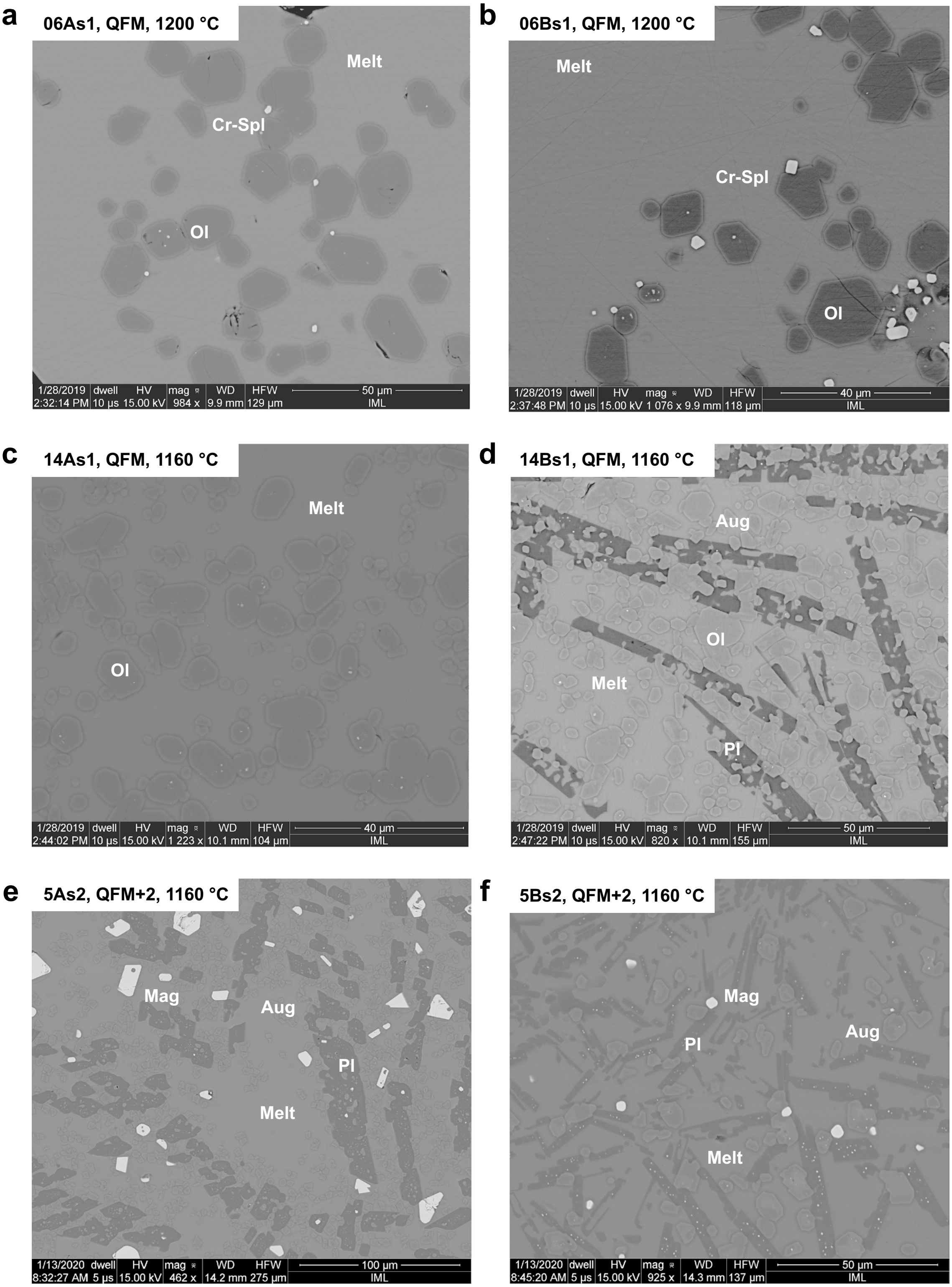

Fig. 2 Back-scattered electron images of selected isothermal experiments. *Ol* olivine; *Cr-Spl* Cr-spinel; *Aug* augite; *Pl* plagioclase; *Mag* magnetite

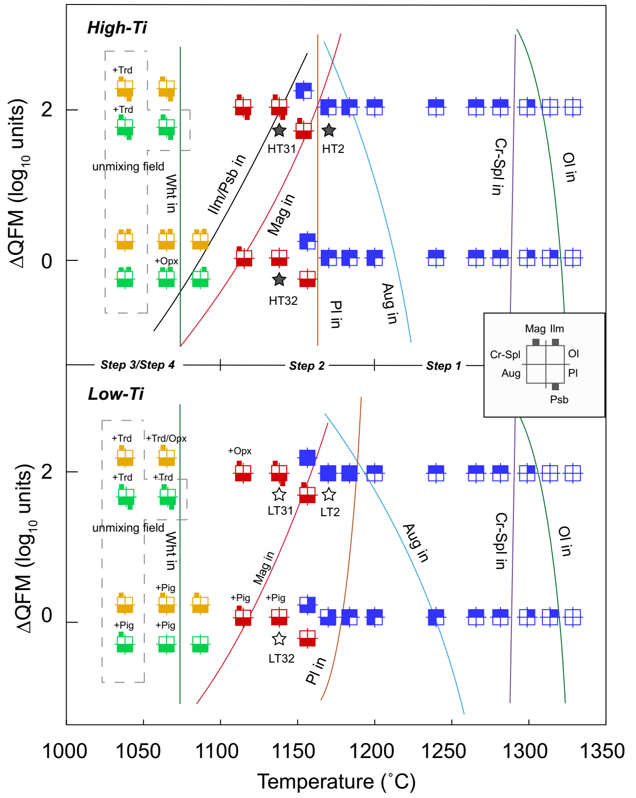

Fig. 3 Phase relations as a function of temperature and fO_2. Blue, red and orange symbols indicate steps 1–3, respectively, in the liquid lines of descent of high-Ti and low-Ti melts (step 1–3); green symbols indicate step 4 experiments testing the development of immiscibility. Gray dashed lines enclose experiments that produced immiscible melts. *Ol* olivine; *Cr-Spl* Cr-spinel; *Aug* augite; *Pl* plagioclase; *Opx* orthopyroxene; *Pig* pigeonite; *Mag* magnetite; *Ilm* ilmenite; *Psb* pseudobrookite; *Tri* tridymite; *Wht* whitlockite

the low-Ti composition begins crystallizing 20 °C hotter than in the high-Ti composition. The cotectic proportion of plagioclase relative to mafic minerals (olivine ± clinopyroxene) is ~ 1:3 when olivine is present and changes to 1:1 when olivine disappears. Trace amount of pigeonite and orthopyroxene are observed at low temperature (1120–1040 °C) in low-Ti experiments at QFM and QFM + 2. No low-Ca pyroxene phase is observed in high-Ti experiments during steps 1–3. Fe–Ti oxides join the liquidus after olivine ± augite ± plagioclase ± low-Ca pyroxene. The liquidus temperature of Fe–Ti oxides is strongly related to fO_2 and melt composition. At QFM, magnetite is the first Fe–Ti oxide phase in both high-Ti and low-Ti experiments appearing at ~ 1120 °C. Ilmenite is stable in high-Ti compositions below ~ 1080 °C but does not crystallize in low-Ti experiments. At QFM + 2, the magnetite liquidus in low-Ti and high-Ti experiments increases 1160 °C, followed by pseudobrookite at 1140 °C. The relative stability of Fe–Ti oxides as a function of fO_2 is consistent with observations in natural rocks (Mullen and McCallum 2013). Whitlockite (too small for chemical analyses) follows Fe–Ti oxides at ~ 1060 °C, regardless of melt composition and fO_2. Subsequently, tridymite appears in both the high-Ti and low-Ti experiments at 1040 °C under QFM and at 1060 °C under QFM + 2, because the residual melt reaches markedly higher SiO_2 contents (see below).

In step 3 and 4 experiments (Table 1), liquid immiscibility between Fe-rich and Si-rich melts develops at 1040 °C in all compositions at both QFM and QFM + 2 (i.e., compositions HT31, HT32, LT31 and LT32). In step 4 experiments at QFM + 2, using starting materials HT31 and LT31, representing residual melts from both series equilibrated at QFM (i.e., runs H101 and L101; Fig. S1, Table 2), immiscibility develops at a slightly higher temperature (1060 °C). This may be due to the high total Fe-contents of the starting compositions and/or the higher $Fe^{3+}/\sum Fe$ at QFM + 2 (Hou et al. 2018). In experiments showing silicate liquid immiscibility, we observe sharp interfaces between the conjugate melts (Figs. 4, S1).

In experiments at QFM and QFM + 2 quenched at 1040 °C, Fe-rich melt droplets range in size from nanometers to several micrometers and are widely distributed within the Si-rich melt. In the interstices between plagioclase crystals, aggregates of Fe-rich melt form irregular melt pools. Fe-rich melt droplets wet plagioclase surfaces with relatively high wetting angles, and are attached to augite and Fe–Ti oxides with lower wetting angles. Whitlockite is usually observed around augite and Fe–Ti oxides, or as feathery fringe microstructures around grain boundaries, as described by Honour et al. (2019a, b). Experiments at QFM + 2 and quenched at 1060 °C (H101 and L101; Table 2) show small Fe-rich droplets (< 0.5 µm) concentrated near or attached to plagioclase.

Melt compositions

The experimental melts produced in steps 1–3 range from basaltic to rhyolitic in composition (Fig. S2). Major element concentrations in homogeneous melts, as well as those in immiscible conjugate melts produced in steps 3 and 4 are shown as a function of temperature in Fig. 5. Due to the small size of Fe-rich droplets, we could only confidently measure the compositions of immiscible melt pairs produced at 1040 °C and QFM (steps 3 and 4), and Si-rich melts at 1060 °C and QFM + 2 (step 4).

Upon cooling, the high-Ti and low-Ti melts show similar compositional trends, because they crystallize similar mineral assemblages. Melt MgO contents are linearly related with experimental temperature. Melt Al_2O_3 and P_2O_5 contents are insensitive to experimental fO_2 conditions. Melt CaO and total alkali ($Na_2O + K_2O$) contents are weakly dependent on fO_2. Melt CaO concentrations at QFM are slightly higher than those at QFM + 2. In both high-Ti and low-Ti experiments, melt CaO content increases steadily

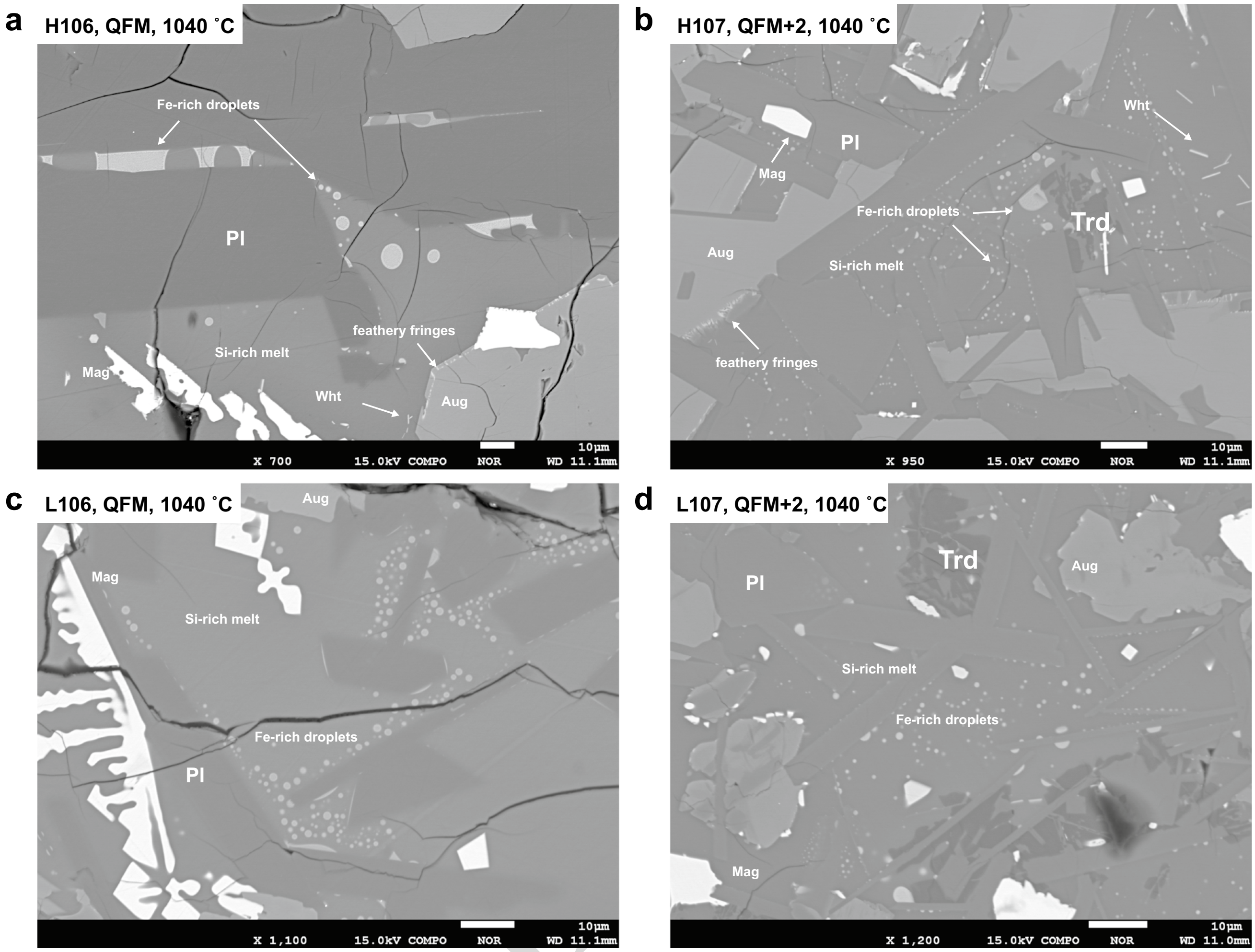

Fig. 4 Back-scattered electron images of selected experimental products showing silicate liquid immiscibility. **a, c** Experiments at QFM showing Fe-rich droplets in Si-rich melt. **b, d** Experiments at QFM + 2 showing smaller Fe-rich droplets within the Si-rich melt and attached to plagioclase crystals. Abbreviations are as in Fig. 3

during early crystallization, reaching a maximum of ~ 13.5 wt% upon augite saturation at ~ 1200–1240 °C, then decreasing gradually to ~ 4.0 wt%. Similarly, Al_2O_3 contents in both the high-Ti and low-Ti melts steadily rise to maximum values of 14.1 wt% at 1160 °C and 15.5 wt% at 1180 °C, respectively, corresponding to the initiation of plagioclase crystallization, and then gradually decrease. The total alkali and P_2O_5 concentrations steadily increase with decreasing temperature. Although whitlockite crystallizes at the lowest experimental temperatures, we do not observe depletion of P_2O_5 in the residual melt.

Due to its critical control on the stability of Fe–Ti oxides, fO_2 has more profound effects on melt TiO_2, FeO, and SiO_2 contents. TiO_2 content is strongly controlled by the crystallization of ilmenite and pseudobrookite, and less so by magnetite. The TiO_2 content of the high-Ti melt reaches a maximum of 4.4 wt% at 1140 °C at QFM, and 3.6 wt% at 1160 °C at QFM + 2, then decreases upon crystallization of Fe–Ti oxides. Similarly, the TiO_2 content of the low-Ti melts reaches a maximum of 2.6 wt% at 1080 °C at QFM before dropping slightly due to magnetite crystallization and a maximum of 2.0 wt% at 1140 °C at QFM + 2, corresponding to the crystallization of pseudobrookite.

The FeO content of the melt evolved differently in the high-Ti and low-Ti experimental series. In the high-Ti experiments, the FeO content of the melt at QFM slightly decreases from ~ 13.0 to ~ 12.0 wt% from 1320 to 1160 °C, increases to 14.1 wt% at 1140 °C then decreases when magnetite crystallizes at 1120 °C. At QFM + 2, the melt FeO content remains constant (at ~ 12.5 wt%) from 1320 to 1160 °C, does not obviously increase just before magnetite saturation (12.7 wt%), then decrease sharply to < 10.0 wt% at 1060 °C. In the low-Ti experiments, the FeO content of the melt at QFM decreases from 11.5 to 9.7 wt% from 1320 to 1175 °C, increases to 12.6 wt% at 1140 °C, then decreases when magnetite crystallizes at 1120 °C. At

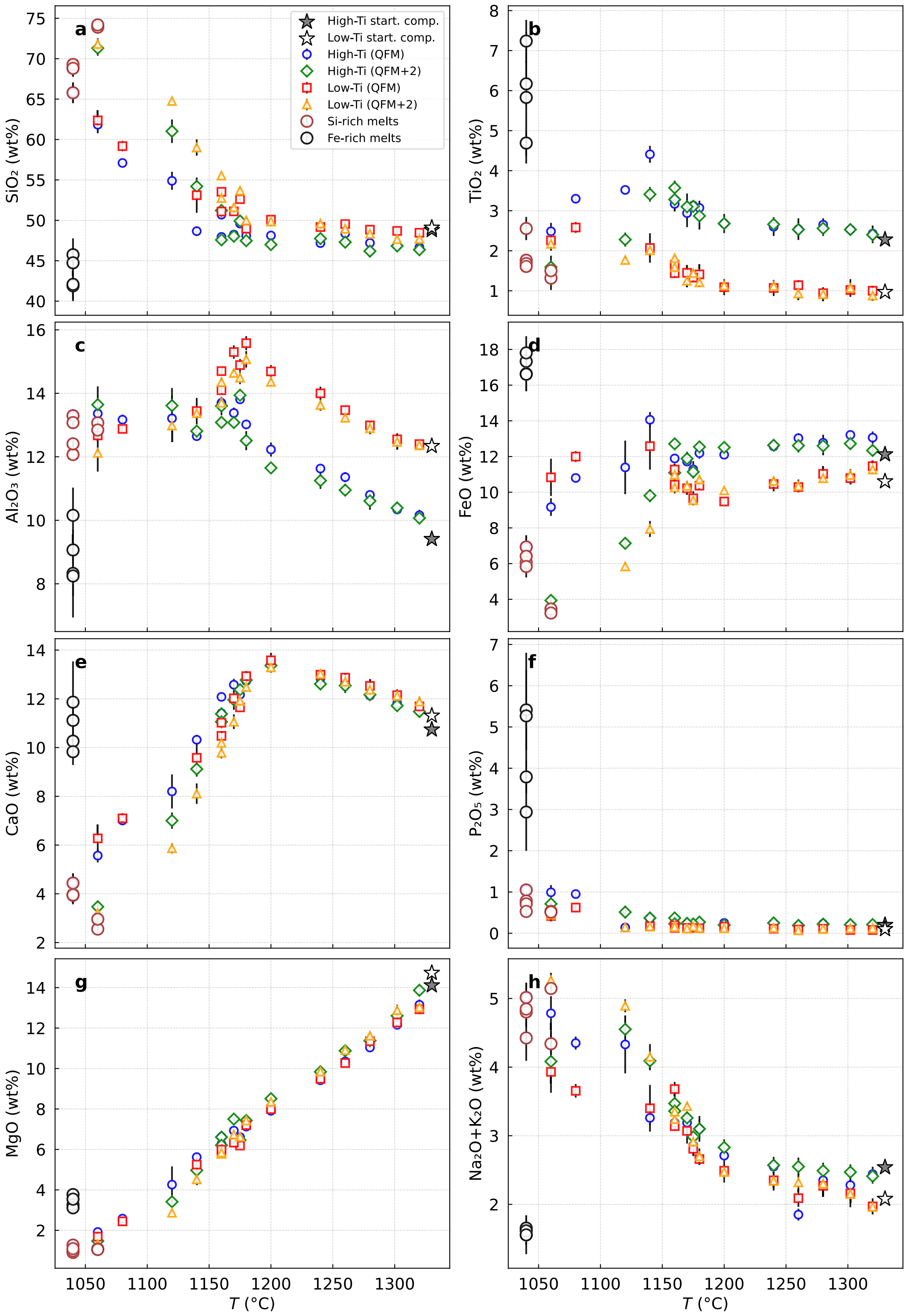

Fig. 5 Binary diagrams of selected major element concentrations in the melt as a function of temperature

QFM + 2, the melt FeO content slightly decreases from liquidus to 1160 °C, then decreases sharply the magnetite crystallization.

Oxygen fugacity also strongly affects the SiO_2 content in the melt. In both the high-Ti and low-Ti melts, SiO_2 content increases slowly but steadily from 1320 to 1140–1160 °C, then more drastically increases below ~ 1140 °C due to Fe–Ti oxide crystallization. In both series, the SiO_2 contents of the melt at QFM + 2 increase more steeply with decreasing temperature than those at QFM, probably due to higher proportions of Fe–Ti oxide crystallization at more oxidizing conditions and higher bulk crystallinity.

The compositions of immiscible melt globules produced at low temperatures (1040–1060 °C in steps 3 and 4) from the high-Ti and low-Ti melts are plotted against melt SiO_2 content in Fig. 6, alongside with the homogeneous melts produced at higher temperatures. Major and minor elements show different degrees of enrichment/depletion in the two immiscible melts. Si-rich melts (65.8–74.2 wt% SiO_2, 3.2–6.9 wt% FeO) are enriched in Al_2O_3 and total alkalis, whereas their conjugate Fe-rich melts (41.9–45.7 wt% SiO_2, 16.6–17.8 wt% FeO) are enriched in TiO_2, CaO, and P_2O_5.

By plotting the degree of polymerization of the silicate melts (NBO/T, [the ratio of non-bridging oxygens to tetrahedrally coordinated network-forming cations, i.e., T = Si + Al + P + Ti; Mysen 1983) against experimental temperature (Fig. 7), we observe that the immiscible melts produced in this study plot near the binodal surface defined by Charlier and Grove (2012), although the binodal apex might be at a slightly higher temperature here (~ 1060 °C at NBO/T ≈ 0.5). Furthermore, the compositions of the last homogeneous melts produced before attaining immiscibility in both the high-Ti and low-Ti series are compositionally similar to the first (i.e. highest-temperature) immiscible Si-rich melts. This is because both compositional trends intersect the binodal nearly tangentially and towards low NBO/T values as previously reported in other tholeiitic settings (Charlier et al. 2011, 2013; Namur et al. 2011; 2012a).

Olivine

Olivine compositions are reported in the Appendix and shown in Fig. 8. Olivine is present in experiments performed at 1320–1160 °C (Table 2). The forsterite content of olivine [Fo = molar Mg/(Mg + Fe)] does not clearly differ between the high-Ti and low-Ti series. In the high-Ti experiments, olivine Fo content ranges from Fo_{87} to Fo_{79} at QFM and from Fo_{89} to Fo_{82} at QFM + 2 (Fig. 8a). This difference is likely due to the higher $Fe^{3+}/\sum Fe$ of the equilibrium melt. In low-Ti experiments, olivine Fo content varies from Fo_{89} to Fo_{78} at QFM and from Fo_{91} to Fo_{83} at QFM + 2. The relationship between olivine Fo content and the Mg# of the coexisting liquid (= molar Mg/[Mg + Fe^{2+}] accounting for ferrous iron in the liquid; Kress and Carmichael 1991) is comparable for both high-Ti and low-Ti compositions (Fig. 8b). Olivine-melts K_D^{Fe-Mg} values range between 0.26 and 0.33, consistent with previous studies (Roeder and Emslie 1970; Toplis 2005; Blundy et al. 2020).

Pyroxene

The high-Ti and low-Ti compositions crystallize augite, and trace amounts of low-Ca pyroxene, orthopyroxene and pigeonite (Fig. 9a). Augite compositional ranges are similar in both magma series: $Wo_{37–45}En_{40–51}Fs_{4–20}$ and $Wo_{41–47}En_{40–50}Fs_{6–13}$ at QFM and QFM + 2, respectively, in high-Ti experiments, and $Wo_{28–43}En_{38–52}Fs_{6–30}$ and $Wo_{38–45}En_{44–51}Fs_{5–12}$ at QFM and QFM + 2, respectively, in low-Ti experiments (Fig. 9a). We calculated pyroxene ferric and ferrous iron contents using the stoichiometric method of Lindsley (1983) and then pyroxene Mg# accordingly. Pyroxene Mg# is positively correlated with temperature, and pyroxenes at QFM + 2 have generally higher Mg# than those at QFM (Fig. 9b). Pyroxene-melt K_D^{Fe-Mg} values are 0.27 ± 0.08 in both the high-Ti and low-Ti compositions (Fig. 9c), consistent with those reported by Toplis and Carroll (1995) for tholeiitic basalts.

Plagioclase

Plagioclase compositions are reported in the Appendix and shown in Fig. 10. Plagioclase compositions (An content = molar Ca/[Ca + Na]) range from An_{72} to An_{58} at QFM and from An_{67} to An_{57} at QFM + 2 in high-Ti experiments, and from An_{78} to An_{70} at QFM and from An_{76} to An_{73} at QFM + 2 in low-Ti experiments. In low-temperature experiments (< 1080 °C), plagioclase crystals are typically small (< 2–3 μm) and locally zoned, inhibiting accurate measurement of their rim composition; therefore, the reported An contents for those experiments are probably slightly elevated because they include both core and rim compositions. Plagioclase in low-Ti experiments start crystallizing earlier (20 °C hotter) than in high-Ti experiments and from a melt with higher CaO- and lower Na_2O-contents (i.e., higher Ca/Na ratio; Fig. 10b). The An content at the plagioclase liquidus is also higher in low-Ti experiments.

Cr-spinel and Fe–Ti oxides

Cr-spinel and Fe–Ti oxide compositions are reported in the Appendix. Cr-spinel Cr# (= molar Cr/[Cr + Al]]) ranges from 0.70 to 0.67 at QFM and from 0.68 to 0.53 at QFM + 2 in high-Ti experiments, and from 0.65 to 0.51 at QFM and from 0.59 to 0.45 at QFM + 2 in low-Ti experiments. Cr# is not correlated with temperature.

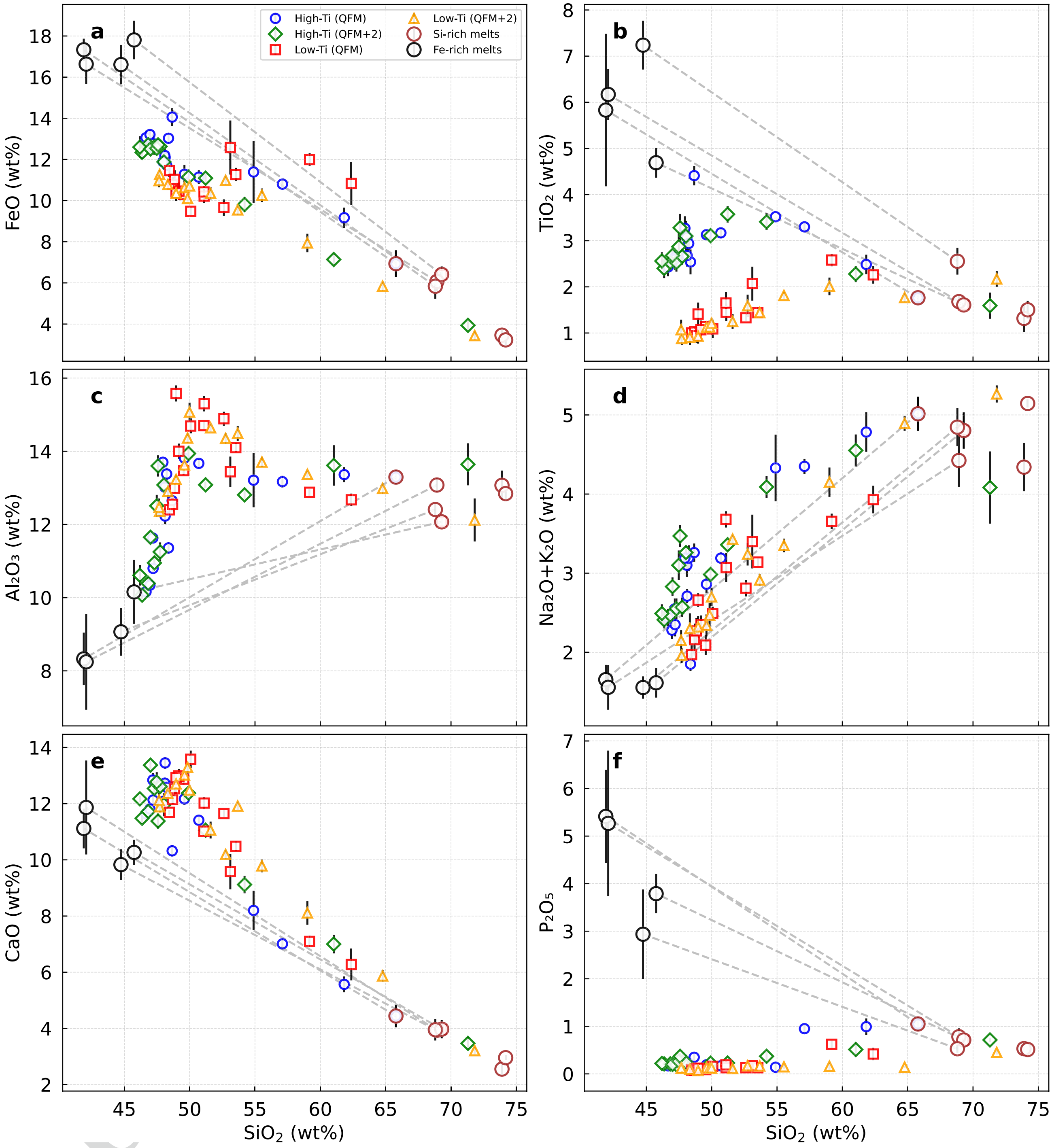

Fig. 6 Major element compositional variations in the melt as a function of melt SiO_2 content (wt%) for high-Ti and low-Ti melts. Immiscible melt pairs are connected by dashed lines

Endmember compositions of Fe–Ti oxides (i.e., X_{Mag}, X_{Hem}, and X_{Psb} for the magnetite–ulvöspinel here ‘magnetite’), hematite–ilmenite (‘ilmenite’), and pseudobrookite–ferropseudobrookite (‘pseudobrookite’) were recalculated following the method of Andersen et al. (1993) (Fig. S3). At a given fO_2, the recalculated magnetite (X_{Mag}) and pseudobrookite (X_{Psb}) components are not correlated with temperature. Pseudobrookite was only observed in QFM + 2 experiments, with compositions $X_{Psb} = 0.69–0.66$ and 0.60 in high-Ti and low-Ti experiments, respectively. Magnetite has compositions of $X_{Mag} = 0.90–0.83$ and 0.92–0.79 in high-Ti and low-Ti experiments at QFM + 2, respectively,

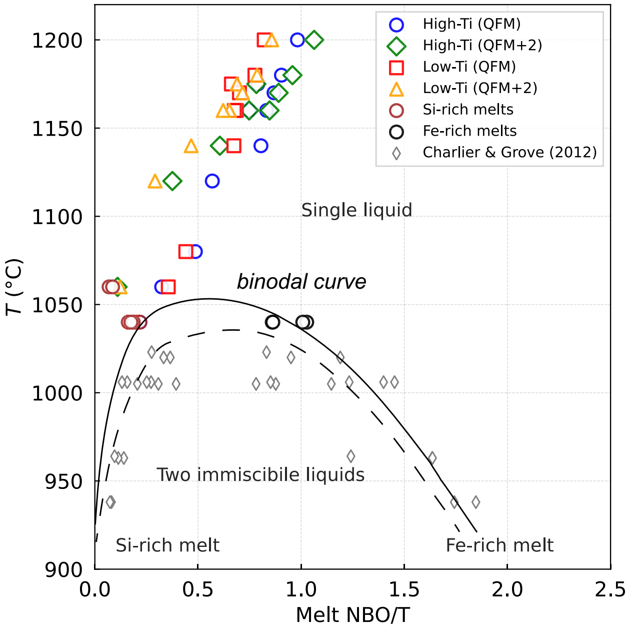

Fig. 7 The degree of melt polymerization (expressed as NBO/T, the ratio of non-bridging oxygens to tetrahedrally coordinated cations, T = Si + Al + P + Ti) versus temperature (< 1200 °C). Immiscible melts from Charlier and Grove (2012) are shown for comparison. The solid and dashed curve are the estimated binodal curve on which our experiments lie and the binodal curve from Charlier and Grove (2012), respectively

whereas at QFM, but lower respective compositions of $X_{Mag} = 0.50–0.43$ and 0.54–0.48 at QFM. Ilmenite was only observed in high-Ti experiments at QFM, with compositions of $X_{Hem} = 0.25–0.19$ that correlate with temperature. Both MgO content in ilmenite and Al_2O_3 content in magnetite decrease with decreasing temperature.

Discussion

Effect of primary magma composition on phase relations and differentiation

As expected, due to their different compositions, our high-Ti and low-Ti melts cooled to crystallize plagioclase and Fe–Ti oxides with different compositions and liquidus temperatures. Nonetheless, both melts have similar MgO and Cr_2O_3 contents and bulk Ca/Al ratios, and thus saturate clinopyroxene of similar compositions at similar liquidus temperatures. The most obvious difference between the high-Ti and low-Ti compositions is the timing of plagioclase saturation. The Ca- and Al-enriched low-Ti melt is closer to the forsterite-anorthite cotectic in the simplified CMAS system than the Na- and Fe-enriched high-Ti melt (Fig. S4; Presnall et al. 1978; Neave et al. 2019). The former meets the cotectic at a lower diopside content and further away from the eutectic point, and therefore, saturates plagioclase at a higher temperature (Fig. S4). Plagioclase An content is controlled by the melt Ca# (= Ca/[Na + Ca]) and Al# (= Al/[Al + Si]) and Ca/Al ratio (Panjasawatwong et al. 1995; Namur et al. 2012b; Neave and Namur 2022;) which are all higher in primitive low-Ti melts than in equivalent high-Ti melts. Consequently, low-Ti melts tend to crystallize plagioclase with higher An content than high-Ti melts (Fig. 10).

The distinct melt compositions also play a role in the saturation of Fe–Ti oxides, although this effect is less pronouncing than that of fO_2. Although our high-Ti and low-Ti melts have indistinguishable magnetite liquidus temperatures at a given fO_2 condition (1120 °C at QFM, 1160 °C at QFM + 2), both are significantly higher than the magnetite liquidus in experiments of Toplis and Carroll (1995; 1096 °C

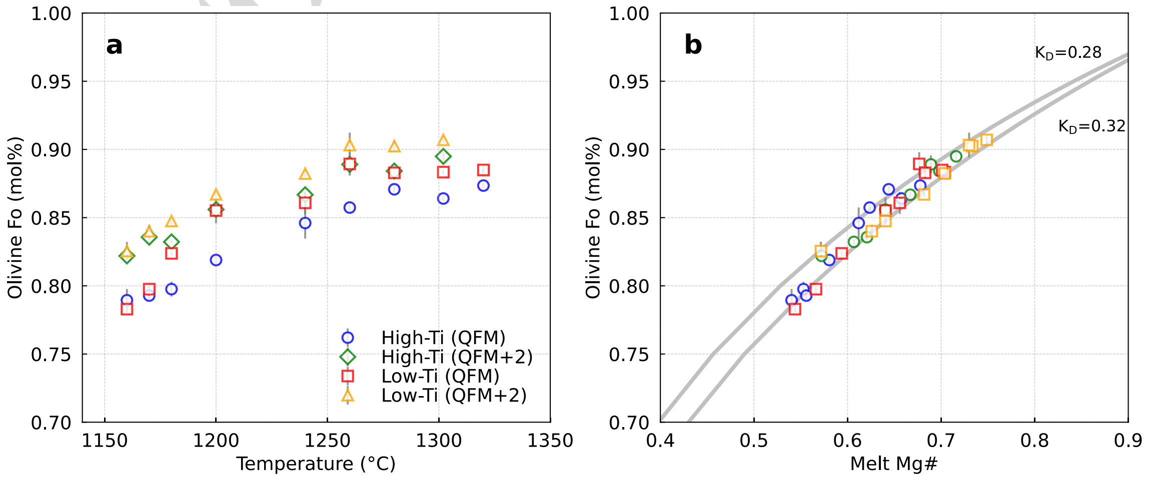

Fig. 8 Olivine forsterite contents as a function of **a** temperature and **b** Mg# of the coexisting melt. The Fe^{2+} content in the melt was calculated following Kress and Carmichael (1991). The grey curves in **b** indicate olivine-melt $K_D^{Fe-Mg} = 0.30 \pm 0.02$

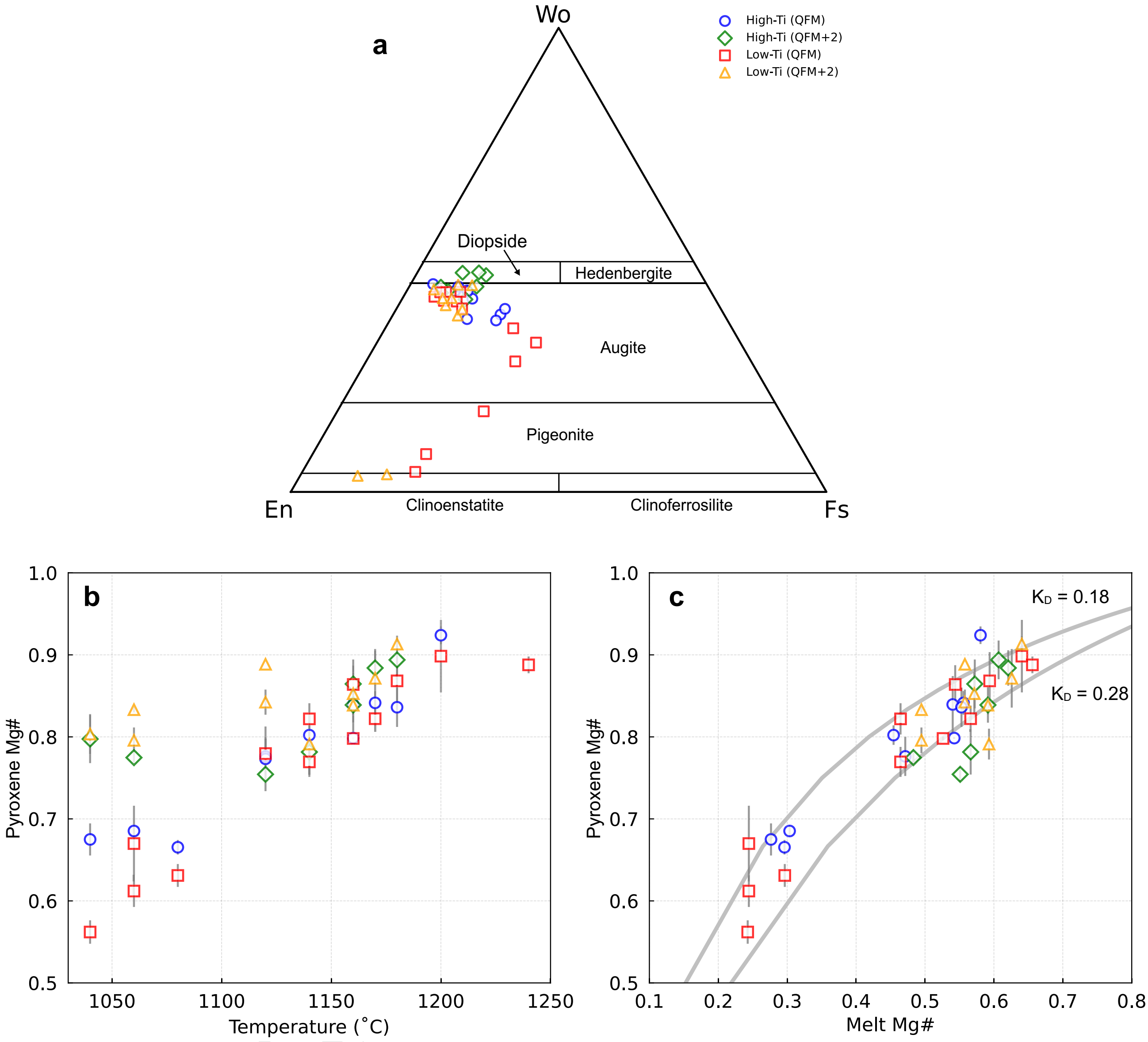

Fig. 9 Experimental pyroxene compositions. **a** Wollastonite (Wo)-enstatite (En)-ferrosilite (Fs) ternary diagram showing the compositions of experimental pyroxenes. **b** Pyroxene Mg# variations as a function of temperature. **c** Pyroxene Fe/Mg equilibrium diagram; gray curves indicate the equilibrium field from Toplis and Carroll (1995; i.e., pyroxene-melt $K_D^{Fe-Mg} = 0.23 \pm 0.05$)

at QFM) and Juster et al. (1989; 1135 °C at QFM + 2.9; 1120 °C at QFM + 1.4). Similarly, two compositions in the experiments of Snyder et al. (1993) have different magnetite liquidi: 1130 °C at QFM in a relatively FeO and TiO_2-rich composition (17.3 wt% FeO, 3.8 wt% TiO_2) and 1109 °C at QFM in a relatively FeO and TiO_2-depleted composition (14.3 wt% FeO, 2.3 wt% TiO_2). Toplis et al. (1994) proposed that the progressive addition of phosphorus may destabilize magnetite under oxidizing conditions; however, is inconsistent with our experiments and those of Snyder et al. (1993), perhaps implying that the magnetite liquidus is controlled by a complex dependence on melt FeO, TiO_2, P_2O_5 and SiO_2 contents and fO_2 (Ariskin and Barmina 1999). The ilmenite crystallization is also affected by the melt TiO_2 content (Toplis and Carroll 1995); indeed, ilmenite did not saturate in the low-Ti melts, which only crystallized pseudobrookite at QFM + 2.

The most representative feature of tholeiitic magmas prior to the saturation of Fe–Ti oxides is the progressive enrichment of FeO in the evolved melt (less than ~ 6 wt% MgO; e.g., Grove and Bryan 1983; Toplis and Carroll 1995; Juster et al. 1989; Snyder et al. 1993). However, compared to the experiments of Toplis and Carroll (1995) and Snyder et al. (1993), our high-Ti and low-Ti melts do not reach high

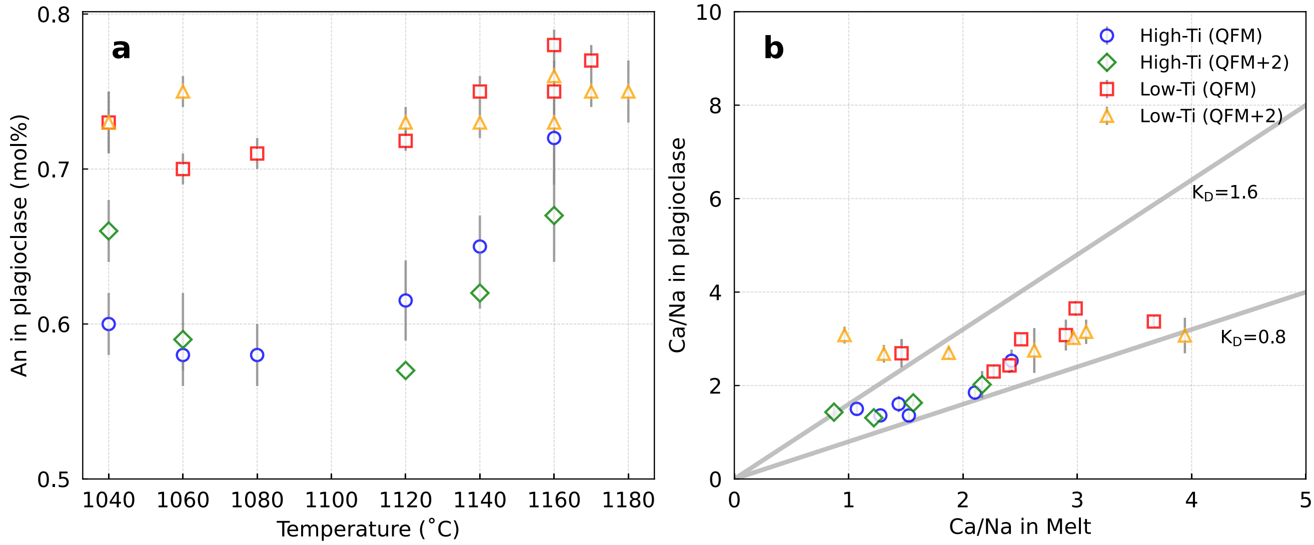

Fig. 10 **a** Experimental plagioclase An content variations as a function of temperature. **b** Ca/Na exchange between plagioclase and melt; gray lines indicate the equilibrium field from Toplis and Carroll (1995; i.e., plagioclase-melt $K_D^{Ca\text{–}Na} = 0.8\text{–}1.6$)

FeO enrichments (up to ~ 18 wt%; Toplis and Carroll 1995) at similar fO_2. This is because we saturate Fe–Ti oxides at much higher temperatures, and likely also due to the significantly higher FeO concentrations in their starting compositions and the higher cotectic proportions of plagioclase in their cumulates during crystallization. For instance, our starting compositions for step 2 contain ~ 6.5 wt% MgO and only ~ 10 wt% FeO, concentrations that were generated by the protracted fractionation of mafic olivine ± clinopyroxene, compared to 13–15 wt% FeO at similar MgO concentrations in the bulk compositions of Toplis and Carroll (1995) and Snyder et al. (1993). Furthermore, the cotectic proportion of plagioclase relative to mafic minerals (olivine ± clinopyroxene) in the experiments of Toplis and Carroll (1995) is ~ 3:1 when only olivine and plagioclase are present, but progressively changes to 2:1 when clinopyroxene crystallizes, and the proportion is roughly 2:1 in the experiments of Snyder et al. (1993). In contrast, our high-Ti and low-Ti melts crystallize plagioclase and augite in the proportion 1:1.

Beside FeO enrichment, TiO_2 enrichment in tholeiitic melts is also observed before Fe–Ti oxides crystallized. Because Ti is relatively incompatible in tholeiitic melts, the maximum TiO_2 enrichment in the melt is related to the TiO_2 content of the parental melt and the liquidus temperatures of Fe–Ti oxides. This is illustrated by the fact that high-Ti melts have higher TiO_2 concentration than low-Ti melts before Fe–Ti oxide saturation (i.e., ilmenite and pseudobrookite). We note that no significant TiO_2 depletion is observed in our low-Ti melts at QFM due to the absence of ilmenite crystallization. This supports the notion that a low-Ti composition could evolve to a high-Ti composition if Fe–Ti oxide saturation is delayed late during differentiation (Hou et al. 2011).

Effect of fO_2 on phase relations and differentiation path

Changing fO_2 significantly affects Fe–Ti oxide phase relations but has only minor effects on silicates. Consistent with previous experiments showing that increasing fO_2 expands the stability field of magnetite (Toplis and Carroll 1995; Snyder et al. 1993; Ariskin and Barmina 1999), the magnetite liquidus in our experiments increases by ~ 40 °C between QFM and QFM + 2 in both the high-Ti and low-Ti compositions. Increasing fO_2 also increases X_{Mag} component of magnetite and causes Al_2O_3-bearing pseudobrookite to form rather than ilmenite. These changes in the stability of Fe–Ti oxides at different fO_2 will thus have significant effect on melt FeO and SiO_2 contents. Figure 11 shows the melt FeO/MgO ratio as a function of SiO_2 content. Because the high-Ti and low-Ti melts follow a similar differentiation trend in terms of MgO concentration (i.e., $dMgO/dT \approx 0.04$ wt%/°C), the observed change of FeO/MgO with SiO_2 content in our experimental melts is directly related to the degree of FeO depletion under different fO_2 conditions. Both high-Ti and low-Ti melts follow a tholeiitic trend at QFM, but a calc-alkaline trend at QFM + 2 due to the early crystallization of high X_{Mag} magnetite. We note, however, that adding water in natural systems may have a similar effect by delaying plagioclase crystallization (Mandler et al. 2014; Almeev et al. 2012). For comparison, experiments on FeO-rich melts coexisting only with low X_{Mag} magnetite at QFM-1 to QFM + 1 (Toplis and Carroll 1995) evolve uniquely within the tholeiitic field (Fig. 11).

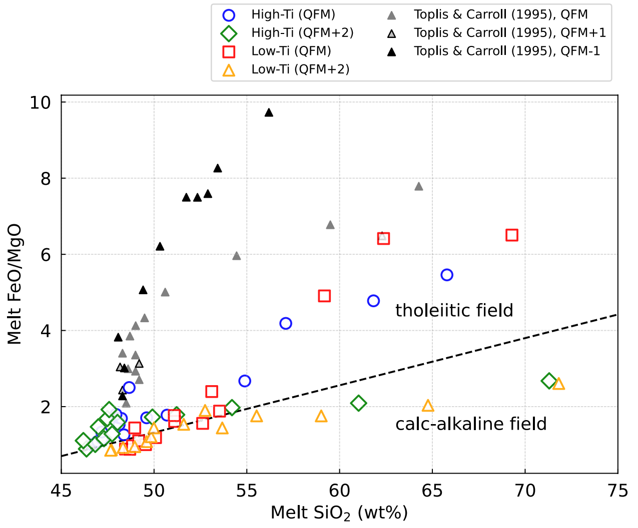

Fig. 11 The relation between the FeO/MgO weight ratio in the melt and melt SiO$_2$ content. The dashed line indicates the boundary between the calc-alkaline and tholeiitic fields after Miyashiro (1974). Experimental melts (fO_2: QFM-1 to QFM + 1) from Toplis and Carroll (1995) are shown for comparison

Comparison between low-pressure liquid lines of descent and natural lavas

Here, we use our experimental data to discuss the low-pressure differentiation of natural lavas in LIPs. We choose the Emeishan LIP as an example due to the considerable amount of data on those natural lavas and because our starting materials were selected based on them. However, we note that Emeishan LIP magmas may have differentiated at higher pressure (Tao et al. 2015) and that the system may also have been slightly hydrous (Liu et al. 2017).

Figure 12 compares our experimental liquid lines of descent (LLDs) with a compilation of Emeishan high-Ti and low-Ti lavas. Overall, our high-Ti LLDs only partly overlap with observed high-Ti lavas, whereas our low-Ti LLDs match the low-Ti lavas relatively well in terms of TiO$_2$, Al$_2$O$_3$, and SiO$_2$. This mismatch with the natural lavas may be related to the differences in differentiation conditions (pressure, water content, fO_2), source heterogeneities and perhaps mineral accumulations (i.e., pyroxene, plagioclase and Fe–Ti oxide) in the natural rocks; therefore, the lavas may not represent true liquid compositions. The CaO contents and CaO/Al$_2$O$_3$ ratios of natural lavas are often lower than those of our experimental melts, likely reflecting the pressure effect on the stability of clinopyroxene: high-pressure conditions favor the crystallization of clinopyroxene, decreasing the melt CaO content (Villiger et al. 2004, 2007). Alternatively, these low-CaO lavas could also be explained by mixing between the primitive and evolved. Furthermore, natural lavas often have higher FeO contents than our experimental melts (< 7 wt% MgO), although this is probably not caused by the early crystallization of plagioclase (see above discussion above), because high pressure or slightly hydrous conditions, that may be realistic for the Emeishan LIP (Tao et al. 2015; Liu et al. 2017; Ganino et al. 2008), would suppress the plagioclase crystallization and delay or inhibit the enrichment of the melt FeO. Thus, the observed difference between the FeO contents of the natural lavas with our experimental melts could result from three processes. (1) The natural lavas may have evolved from a primitive melt with a higher FeO content than our selected compositions; indeed, the compiled database exhibits a broad range of primitive FeO contents (Fig. 1c). (2) The lavas may have evolved from a multi-component source. For example, the partial melting of a pyroxenitic source can produce parental melts more enriched in FeO than those produced by the melting of a peridotitic source (Lambart et al. 2013). This is supported by the multivariate trace element and radiogenic isotopic composition of primitive picrites and olivines in the Emeishan LIP (e.g., Kamenetsky et al. 2012); (3) Finally, the accumulation of dense magnetite phases that crystallized at high fO_2 conditions (Howarth et al. 2013) may have increased the lavas' FeO contents, consistent with previous estimates of high fO_2 conditions for the Emeishan lavas (Cao and Wang 2022; Bai et al. 2019).

Predicting the onset of silicate liquid immiscibility

Liquid immiscibility is known to occur during the late-stage fractionation of basalts and has been identified in many layered intrusions related to LIPs (Veksler and Charlier 2015), such as the Skaergaard intrusion (Holness et al. 2011; Humphreys 2011; Jakobsen et al. 2005; McBirney and Nakamura 1974), the Sept Iles intrusion (Charlier et al. 2011; Namur et al. 2012a; Keevil et al. 2020), the Bushveld Complex (Fischer et al. 2016; VanTongeren and Mathez 2012; Yuan et al. 2017) and the Panzhihua intrusion (Zhou et al. 2013; Wang et al. 2018; 2021). It is commonly accepted that unmixing begins at temperatures around 1040 °C (Philpotts 2008; Charlier and Grove 2012; Hou et al. 2018; Honour et al. 2019a, 2019b), although Hou and Veksler (2015) also produced super-liquidus immiscibility at temperature up to 1200 °C. Our and Charlier and Grove's (2012) experiments suggest that immiscibility does not require extreme iron enrichments (> 20 wt%; Veksler 2009) and can even start after the crystallization of magnetite, which depletes FeO in the residual melt. Increased TiO$_2$, P$_2$O$_5$ and alkali contents have also been shown to promote immiscibility by expanding the two liquids field (Charlier and Grove 2012). Increasing fO_2 and aH_2O may also widen the immiscibility field (Hou et al. 2018; Naslund 1983).

Considering the energy of the entire system, when immiscibility occurs, the total Gibbs free energy of mixing (G^{mix})

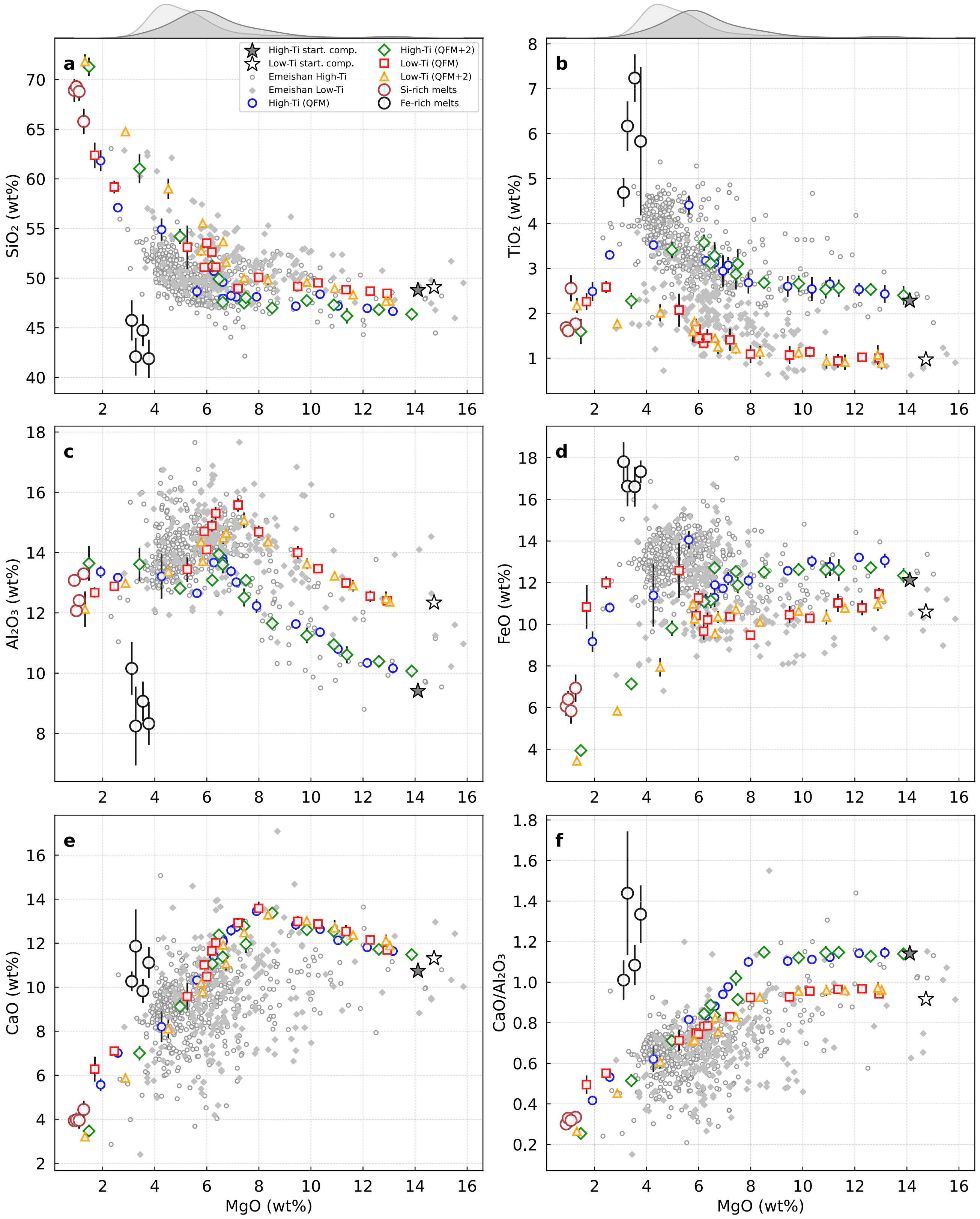

Fig. 12 Harker diagrams showing the evolution of experimental melts obtained in this study compared to natural lavas from the Emeishan LIP (the compiled dataset is listed in the caption to Fig. 1). The histograms atop the uppermost panels show the distribution of MgO contents in natural Emeishan high-Ti and low-Ti lavas

for a single liquid prior to unmixing is higher than the sum of G^{mix} for the immiscible pair, with G^{mix} being identical for the coexisting immiscible pair (Ghiorso and Carmichael 1980; Ghiorso et al. 1983):

$$\Delta G^{\mathrm{mix}} = G^{\mathrm{ideal}} + G^{\mathrm{excess}} \tag{1}$$

$$\Delta G^{\mathrm{mix}}_{\text{single liquid}} > \Delta G^{\mathrm{mix}}_{\mathrm{A}} + \Delta G^{\mathrm{mix}}_{\mathrm{B}} \tag{2}$$

with A and B representing the immiscible pairs. The first derivative of the Gibbs free energy of mixing ($\partial G^{\mathrm{mix}}/\partial n_k$, where n_k is the moles of the component k) with respect to any component in the silicate liquid will thus change from negative to positive when unmixing occurs (Fig. 13). Ghiorso and Carmichael (1980) defined 17 independent components (see their Table 1) to quantitatively calculate G^{mix} based on the interaction energies between those components in the silicate liquids. Thus $\partial G^{\mathrm{mix}}/\partial n_k$ can be equated to $RT\ln a_k$ as (see Eq. 18 in Ghiorso and Carmichael 1980):

$$\left(\frac{\partial G^{\mathrm{mix}}}{\partial n_k}\right)_{T,P,n\neq n_k} = RT\ln X_k + RT\ln\gamma_k = RT\ln a_k, \tag{3}$$

where R is the gas constant (8.314 J mol^{-1} K^{-1}), T is the experimental temperature in Kelvin and X_k, γ_k and a_k are the mole fraction, activity coefficient and activity of component k. Ghiorso and Carmichael (1980) gave the example of calculating the first derivative of Gibbs free energy of mixing with respect to the SiO_2 component ($\partial G^{\mathrm{mix}}/\partial nSiO_2$; see their Fig. 2), which can potentially be used to investigate the development of immiscibility by solving the evolution of $aSiO_2$ in the melt upon cooling. When immiscibility develops, $\partial G^{\mathrm{mix}}/\partial nSiO_2$ of the liquid, i.e., $RT\ln aSiO_2$ can be used to define the binodal surface of the immiscible pair (i.e., the width of the binodal surface). We tested Ghiorso and Carmichael's (1980) model, but it did not successfully predict immiscibility in our experiments or other experiments where immiscibility was observed. This is probably due to our still far-from-perfect knowledge of thermodynamics in multi-component silicate melts, precluding the accurate calculation of the activities of their various components.

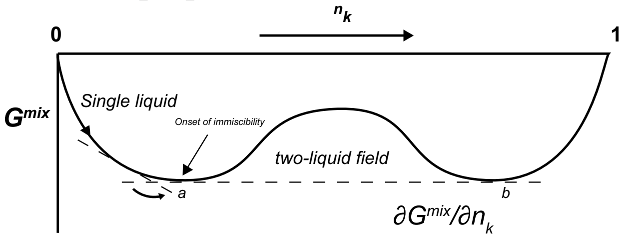

Fig. 13 Sketch of the Gibbs free energy of mixing (G^{mix}) and the change of its first derivative ($\partial G^{\mathrm{mix}}/\partial n_k$) with respect to component k in the system, modified after Ghiorso and Carmichael (1980). a and b indicate where $\partial G^{\mathrm{mix}}/\partial n_k$ changes to 0, i.e., the onset of unmixing and the development of immiscible melt compositions

Here, by analogy to the thermodynamic expression of Ghiorso and Carmichael (1980), we propose a new empirical parameterization to predict immiscibility in silicate melts. Previous studies have found that the sum of the mole percentages of TiO_2, FeO, MgO, CaO and P_2O_5 may effectively distinguish Si-rich and Fe-rich melts (Charlier and Grove 2012; Hou et al 2018; Kamenetsky et al 2013). We thus use this term instead of the mole fraction of the SiO_2 component (as in Ghiorso and Carmichael 1980) to describe the compositional contrast between the two immiscible melts. We performed a polynomial curve fit on all the available experiments with immiscible melts under condition relevant to natural systems. Our best fitting result is:

$$RT\ln X_{SiO_2} = \frac{4.6\times10^{-4}\times\left((-14736.5-\phi)^2-12323.9\times\left(\phi^2\right)\right)}{2.155}, \tag{4}$$

where X_{SiO_2} is the mole percentage of SiO_2 in the liquid and, ϕ is the sum of the mole percentage of oxides dominantly partitioning into the Fe-rich melt, i.e. $X_{TiO_2}+X_{FeO}+X_{MgO}+X_{CaO}+X_{P_2O_5}$. The coefficient of determination (r^2) for this fit is 0.95. The fitted curve covers the calibration range: ϕ = 6.3–67.8 (mol%); T = 938–1053 °C; P from 1 atm to 100 MPa, fO_2 from QFM −6 to QFM + 3.3, 0–2.6 wt% H_2O in the Si-rich melt and 0–1.6 wt% in the Fe-rich melt.

The fitted curve and the experimental data used to calibrate it are shown in Fig. 14. When only miscible melts are considered, the melt gradually evolves towards $TiO_2 + FeO + MgO + CaO + P_2O_5$ depletion in the single-liquid field, reflecting the effect of the fractionation of mafic phases on melt differentiation. We further tested our model on natural immiscible melts hosted in melt inclusions from Siberian Traps (Kamenetsky et al. 2013) and the Bushveld Complex (Fischer et al. 2016); they mostly plot well within the two-liquids field delimited by our fitted binodal surface, supporting the use of the model on natural samples. Some of the data of Bushveld data plot above the binodal surface, possibly due to contamination by the host phase resulting from the small sizes of these melt inclusions, which limit the width of the electron beam. Nonetheless, they still intersect the Fe-rich melt endmember at high $TiO_2 + FeO + MgO + CaO + P_2O_5$. In contrast, the crystallization experiments of Juster et al. (1989) and Toplis and Carroll (1995), which did not develop liquid immiscibility, follow the fractionation trend but correctly plot above the binodal surface on the Si-rich melt endmember.

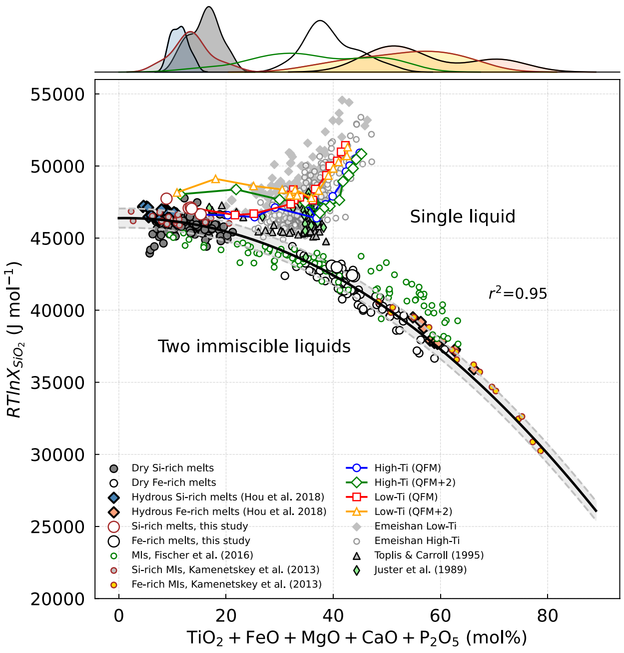

Fig. 14 Parameterization of the binodal surface for immiscible melts in LIPs. The kernel density plot at the top indicates the distribution of experimental and natural immiscible melts. The solid black line represents the best fit of our model and the gray envelope indicates the 1 σ error of our estimation. Experimental data used for fitting include dry immiscibility experiments (this study; Charlier and Grove 2012; Dixon and Rutherford1979; Philpotts and Doyle 1983; Hess et al. 1975; Longhi 1990; Ryerson and Hess 1978, 1980; Hou et al. 2017; Rutherford et al. 1974; Honour et al. 2019a) and hydrous experiments from Hou et al. (2018). Natural melt inclusion (MI) data are from the Siberian Traps, Russia (Kamenetsky et al. 2013) and the Bushveld Complex, South Africa (Fischer et al. 2016); Experimental melts that did not develop immiscibility (Toplis and Carroll 1995; Juster et al. 1989) are shown for comparison

Immiscibility and implications for Fe–Ti ore deposits in LIPs

Immiscibility between Si-rich and Fe-rich melts is often proposed as a mechanism for the origin of Fe–Ti oxide deposits in layered intrusions (e.g., Zhou et al. 2005; 2013; Charlier et al. 2011; Fischer et al. 2016). However, this remains controversial and these Fe–Ti oxide deposits could also be produced by the simple mechanical accumulation of Fe–Ti oxide crystals (e.g., Tegner et al. 2006; Song et al. 2013).

The Panzhihua layered intrusion within the Emeishan LIP hosts one of the largest Fe–Ti oxide ore deposit and is genetically associated with the Emeishan high-Ti lavas (Zhou et al. 2005; Pang et al. 2008). To assess whether natural Emeishan lavas could have developed immiscibility, we apply our model (Eq. 4) to the high-Ti and low-Ti lavas in the database complied in Fig. 14. Both the high-Ti and low-Ti lavas follow trends similar to our experimental melts before they attained immiscibility. The high-Ti lavas eventually intersect our binodal, but this is not the case for the low-Ti lavas. We note that the Emeishan lavas may have been slightly hydrous (Ganino et al; 2008; Liu et al. 2017), which may shift them closer to the binodal, because H_2O depresses the liquidus temperature (Parman and Grove 2004; Médard and Grove 2008). These results suggest that the high-Ti lavas may have developed immiscibility and contributed to the formation of the Fe–Ti oxide ore deposits, as previously proposed by Zhou et al. (2008) and consistent with observations of immiscibility textures in the Emeishan LIP (Liu et al. 2016; Dong et al. 2021; Wang et al. 2018, 2021; Xiong et al. 2021).

Moreover, our experimental results indicate that FeO depletion caused by Fe–Ti oxide crystallization does not hinder the development of immiscibility. This suggests that the formation of Fe–Ti ore could result from a combination of both fractionation and immiscibility. If a magma is buffered at high fO_2, either intrinsically or due to interaction with a sedimentary host (e.g., Ganino et al. 2008) and crystallizes Fe–Ti oxides early, the residual melt may still evolve to develop immiscibility. It is thus probable that early crystallized Fe–Ti oxides would preferentially settle to the bottom of the intrusion/magma chamber, causing the melt to evolve by fractional crystallization and eventually develop liquid immiscibility. The unmixing process would further enrich the accumulated layer of Fe–Ti oxides by downward percolation of the dense immiscible Fe-rich melt or produce Fe–Ti enriched layers at a more evolved stage in upper levels of the intrusion/chamber.

Conclusions

We performed experiments to determine the controls of primitive magma compositions and fO_2 on the liquid lines of descent, phase stability, and compositions of high-Ti and low-Ti LIP basalts. Our results indicate that starting composition affects phase chemistry, whereas fO_2 exerts a major control on the stability and chemistry of Fe–Ti oxides. Both high-Ti and low-Ti magmas can reach the two-liquid field at late stages of differentiation. High fO_2 conditions trigger the early crystallization of Fe–Ti oxides but do not hinder the development of immiscibility. We propose a new empirical parameterization for the binodal surface of the two liquid field in compositional space. Our model successfully replicates unmixing in both experiments and natural melt inclusions. Massive Fe–Ti oxide ores in layered intrusions associated with LIPs may thus form by the segregation of immiscible Fe-rich melts and/or the accumulation of early Fe–Ti oxides during fractionation.

Supplementary Information The online version contains supplementary material available at https://doi.org/10.1007/s00410-022-01990-x.

Acknowledgements We thank J. Berndt and T. D. van Gerve for assistance with microprobe analyses. R. Dennen is thanked for his help in editing the manuscript. We thank Othmar Müntener for editorial handling, Felix Marxer and Edmond Mathez for constructive reviews. The figures in this publication were produced using the Matplotlib python library and Adobe Illustrator. YZ was supported by an ERC Runner-up FWO grant to ON. ON acknowledges support from the KU Leuven through a KU Leuven Starting Grant and a FWO Odysseus project. BC is a Research Associate of the Belgian Fund for Scientific Research-FNRS.

Availability of data and materials Additional data are available as supplementary electronic files.

Declarations

Conflict of interest Not applicable.

References

Almeev RR, Holtz F, Koepke J, Parat F (2012) Experimental calibration of the effect of H_2O on plagioclase crystallization in basaltic melt at 200 MPa. Am Mineral 97(7):1234–1240

Andersen DJ, Lindsley DH, Davidson PM (1993) QUILF: a pascal program to assess equilibria among Fe–Mg–Mn–Ti oxides, pyroxenes, olivine, and quartz. Comput Geosci 19:1333–1350

Arguin JP, Pagé P, Barnes SJ, Yu SY, Song XY (2016) The effect of chromite crystallization on the distribution of osmium, iridium, ruthenium and rhodium in picritic magmas: an example from the Emeishan Large Igneous Province, Southwestern China. J Petrol 57:1019–1048. https://doi.org/10.1093/petrology/egw033

Ariskin AA, Barmina GS (1999) An empirical model for the calculation of spinel-melt equilibria in mafic igneous systems at atmospheric pressure: 2. Fe–Ti oxides. Contrib Mineral Petrol 134(2):251–263

Armstrong JT (1995) Citzaf-a package of correction programs for the quantitative electron microbeam x-ray-analysis of thick polished materials, thin-films, and particles. Microbeam Anal 4:177–200

Bai ZJ, Zhong H, Hu RZ, Zhu WG, Hu WJ (2019) Composition of the chilled marginal rocks of the Panzhihua layered intrusion, Emeishan large igneous province, SW China: implications for parental magma compositions, sulfide saturation history and Fe–Ti oxide mineralization. J Petrol 60:619–648. https://doi.org/10.1093/petrology/egz008

Blundy J, Melekhova E, Ziberna L, Humphreys M, Cerantola V, Brooker RA, McCammon CA, Pichavant M, Ulmer P (2020) Effect of redox on Fe–Mg–Mn exchange between olivine and melt and an oxybarometer for basalts. Contrib Mineral Petrol 175:103. https://doi.org/10.1007/s00410-020-01736-7

Bryan SE, Ernst RE (2008) Revised definition of large Igneous Provinces (LIPs). Earth Sci Rev 86:175–202. https://doi.org/10.1016/j.earscirev.2007.08.008

Campbell IH (2005) Large igneous provinces and the mantle plume hypothesis. Elements 1:265–269

Campbell IH, Griffiths RW (1990) Implications of mantle plume structure for the evolution of flood basalts. Earth Planet Sci Lett 99:79–93. https://doi.org/10.1016/0012-821X(90)90072-6

Cao Y, Wang CY (2022) Contrasting oxidation states of low-Ti and high-Ti magmas control Ni–Cu sulfide and Fe–Ti oxide mineralization in Emeishan Large Igneous Province. Geosci Front 13(6):101434

Charlier B, Grove TL (2012) Experiments on liquid immiscibility along tholeiitic liquid lines of descent. Contrib Mineral Petrol 164:27–44. https://doi.org/10.1007/s00410-012-0723-y

Charlier B, Namur O, Malpas S, de Marneffe C, Duchesne JC, Vander Auwera J, Bolle O (2010) Origin of the giant Allard Lake ilmenite ore deposit (Canada) by fractional crystallization, multiple magma pulses and mixing. Lithos 117(1–4):119–134

Charlier B, Namur O, Toplis MJ, Schiano P, Cluzel N, Higgins MD, Auwera JV (2011) Large-scale silicate liquid immiscibility during differentiation of tholeiitic basalt to granite and the origin of the Daly gap. Geology 39:907–910. https://doi.org/10.1130/G32091.1

Charlier B, Namur O, Grove TL (2013) Compositional and kinetic controls on liquid immiscibility in ferrobasalt–rhyolite volcanic and plutonic series. Geochim Cosmochim Acta 113:79–93

Chung S-L, Jahn B (1995) Plume-lithosphere interaction in generation of the Emeishan flood basalts at the Permian-Triassic boundary. Geology 23:889–892

Cox KG, MacDonald R, Hornung G (1967) Geochemical and petrographic provinces in the Karroo basalts of southern Africa. Am Mineral 52:1451–1474

Dixon S, Rutherford MJ (1979) Plagiogranites as late-stage immiscible liquids in ophiolite and mid-ocean ridge suites: an experimental study. Earth Planet Sci Lett 45(1):45–60

Dong H, Wang K, Liu B (2021) Amphibole geochemistry of the Baima layered intrusion, SW China: Implications for the evolution of interstitial liquid and the origin of Fe–Ti oxide ores. Ore Geol Rev 139:104436

Ernst RE (2014) Large igneous provinces. Cambridge University Press

Fan H-P, Zhu W-G, Li Z-X, Zhong H, Bai Z-J, He D-F, Chen C-J, Cao C-Y (2013) Ca. 1.5Ga mafic magmatism in South China during the break-up of the supercontinent Nuna/Columbia: the Zhuqing Fe–Ti–V oxide ore-bearing mafic intrusions in western Yangtze Block. Lithos 168–169:85–98. https://doi.org/10.1016/j.lithos.2013.02.004

Fischer LA, Wang M, Charlier B, Namur O, Roberts RJ, Veksler IV, Cawthorn RG, Holtz F (2016) Immiscible iron- and silica-rich liquids in the Upper Zone of the Bushveld Complex. Earth Planet Sci Lett 443:108–117. https://doi.org/10.1016/j.epsl.2016.03.016

Freise M, Holtz F, Nowak M, Scoates JS, Strauss H (2009) Differentiation and crystallization conditions of basalts from the Kerguelen large igneous province: an experimental study. Contrib Mineral Petrol 158(4):505–527

Ganino C, Arndt NT, Zhou M-F, Gaillard F, Chauvel C (2008) Interaction of magma with sedimentary wall rock and magnetite ore genesis in the Panzhihua mafic intrusion, SW China. Miner Deposita 43(6):677. https://doi.org/10.1007/s00126-008-0191-5

Ghiorso MS, Carmichael ISE (1980) A regular solution model for met-aluminous silicate liquidus: applications to geothermometry, immiscibility, and the source regions of basic magmas. Contrib Mineral Petrol 71:323–342

Ghiorso MS, Carmichael IS, Rivers ML, Sack RO (1983) The Gibbs free energy of mixing of natural silicate liquids; an expanded regular solution approximation for the calculation of magmatic intensive variables. Contrib Mineral Petrol 84(2):107–145

Grove TL (1981) Use of FePt alloys to eliminate the iron loss problem in 1 atmosphere gas mixing experiments: theoretical and practical considerations. Contr Mineral Petrol 78:298–304. https://doi.org/10.1007/BF00398924

Grove TL, Bryan WB (1983) Fractionation of pyroxene-phyric MORB at low pressure: an experimental study. Contrib Mineral Petrol 84(4):293–309

Hanski E, Kamenetsky VS, Luo ZY, Xu YG, Kuzmin DV (2010) Primitive magmas in the Emeishan Large Igneous Province, southwestern China and northern Vietnam. Lithos 119:75–90. https://doi.org/10.1016/j.lithos.2010.04.008

He B, Xu Y-G, Zhong Y-T, Guan J-P (2010) The Guadalupian-Lopingian boundary mudstones at Chaotian (SW China) are clastic rocks rather than acidic tuffs: implication for a temporal coincidence between the end-Guadalupian mass extinction and the Emeishan volcanism. Lithos 119:10–19

Heinonen JS, Brown EL, Turunen ST, Luttinen AV (2022) Heavy rare earth elements and the sources of continental flood basalts. J Petrol 63(10):egac098

Hess PC, Rutherford MJ, Guillemette RN, Ryerson FJ, Tuchfeld HA (1975) Residual products of fractional crystallisation of lunar magmas-an experimental study. Proc Lunar Planet Sci Conf 6:895–909

Holness MB, Stripp G, Humphreys MCS, Veksler IV, Nielsen TF, Tegner C (2011) Silicate liquid immiscibility within the crystal mush: late-stage magmatic microstructures in the Skaergaard intrusion, East Greenland. J Petrol 52:175–222

Honour VC, Holness MB, Partridge JL, Charlier B (2019a) Microstructural evolution of silicate immiscible liquids in ferrobasalts. Contrib Mineral Petrol 174:77. https://doi.org/10.1007/s00410-019-1610-6

Honour VC, Holness MB, Charlier B, Piazolo SC, Namur O, Prosa TJ, Martin I, Helz RT, Maclennan J, Jean MM (2019b) Compositional boundary layers trigger liquid unmixing in a basaltic crystal mush. Nat Commun 10(1):1–8

Hou T, Veksler IV (2015) Experimental confirmation of high-temperature silicate liquid immiscibility in multicomponent ferrobasaltic systems. Am Mineral 100:1304–1307

Hou T, Zhang Z, Kusky T, Du Y, Liu J, Zhao Z (2011) A reappraisal of the high-Ti and low-Ti classification of basalts and petrogenetic linkage between basalts and mafic–ultramafic intrusions in the Emeishan Large Igneous Province, SW China. Ore Geol Rev 41(1):133–143

Hou T, Charlier B, Namur O, Schütte P, Schwarz-Schampera U, Zhang Z, Holtz F (2017) Experimental study of liquid immiscibility in the Kiruna-type Vergenoeg iron–fluorine deposit, South Africa. Geochim Cosmochim Acta 203:303–322

Hou T, Charlier B, Holtz F, Veksler I, Zhang Z, Thomas R, Namur O (2018) Immiscible hydrous Fe–Ca–P melt and the origin of iron oxide-apatite ore deposits. Nat Commun 9:1415. https://doi.org/10.1038/s41467-018-03761-4

Howarth GH, Prevec SA, Zhou M-F (2013) Timing of Ti-magnetite crystallisation and silicate disequilibrium in the Panzhihua mafic layered intrusion: implications for ore-forming processes. Lithos 170–171:73–89. https://doi.org/10.1016/j.lithos.2013.02.020

Humphreys MC (2011) Silicate liquid immiscibility within the crystal mush: evidence from Ti in plagioclase from the Skaergaard intrusion. J Petrology 52:147–174

Jakobsen JK, Veksler IV, Tegner C, Brooks CK (2005) Immiscible iron- and silica-rich melts in basalt petrogenesis documented in the Skaergaard intrusion. Geology 33:885–888

Juster TC, Grove TL, Perfit MR (1989) Experimental constraints on the generation of FeTi basalts, andesites, and rhyodacites at the Galapagos Spreading Center, 85°W and 95°W. J Geophys Res Solid Earth 94:9251–9274

Kamenetsky VS, Chung S-L, Kamenetsky MB, Kuzmin DV (2012) Picrites from the Emeishan Large Igneous Province, SW China: a compositional continuum in primitive magmas and their respective mantle sources. J Petrol 53:2095–2113. https://doi.org/10.1093/petrology/egs045

Kamenetsky VS, Charlier B, Zhitova L, Sharygin V, Davidson P, Feig S (2013) Magma chamber–scale liquid immiscibility in the Siberian Traps represented by melt pools in native iron. Geology 10:1091–1094

Keevil HA, Namur O, Holness MB (2020) Microstructures and late-stage magmatic processes in layered mafic intrusions: symplectites from the Sept Iles Intrusion, Quebec, Canada. J Petrol. https://doi.org/10.1093/petrology/egaa071

Kress VC, Carmichael ISE (1991) The compressibility of silicate liquids containing Fe$_2$O$_3$ and the effect of composition, temperature, oxygen fugacity and pressure on their redox states. Contrib Mineral Petrol 108:82–92. https://doi.org/10.1007/BF00307328

Lambart S, Laporte D, Schiano P (2013) Markers of the pyroxenite contribution in the major-element compositions of oceanic basalts: review of the experimental constraints. Lithos 160:14–36

Li X, Zhang C, Almeev RR, Holtz F (2020) GeoBalance: an Excel VBA program for mass balance calculation in geosciences. Geochem 80(2):125629

Lindsley D (1983) Pyroxene thermometry. Am Mineral 68:477–493

Liu PP, Zhou MF, Ren Z, Wang CY, Wang K (2016) Immiscible Fe-and Si-rich silicate melts in plagioclase from the Baima mafic intrusion (SW China): implications for the origin of bi-modal igneous suites in large igneous provinces. J Asian Earth Sci 127:211–230

Liu J, Xia QK, Kuritani T, Hanski E, Yu HR (2017) Mantle hydration and the role of water in the generation of large igneous provinces. Nat Commun 8:1824. https://doi.org/10.1038/s41467-017-01940-3

Longhi J (1990) Silicate liquid immiscibility in isothermal crystallisation experiments. Proc Lunar Planet Sci Conf 20:13–24

Mandler BE, Donnelly-Nolan JM, Grove TL (2014) Straddling the tholeiitic/calc-alkaline transition: the effects of modest amounts of water on magmatic differentiation at Newberry Volcano, Oregon. Contrib Mineral Petrol 168(4):1066. https://doi.org/10.1007/s00410-014-1066-7

Marsh JS, Ewart A, Milner SC, Duncan AR, Miller RM (2001) The Etendeka Igneous Province: magma types and their stratigraphic distribution with implications for the evolution of the Paraná-Etendeka flood basalt province. Bull Volcanol 62:464–486. https://doi.org/10.1007/s004450000115

McBirney AR, Nakamura N (1974) Immiscibility in late-stages magmas of the Skaergaard intrusion. Yearbook Carnegie Inst Wash 73:348–352

Médard E, Grove TL (2008) The effect of H$_2$O on the olivine liquidus of basaltic melts: experiments and thermodynamic models. Contrib Mineral Petrol 155(4):417–432

Miyashiro A (1974) Volcanic rock series in island arcs and active continental margins. Am J Sci 274(4):321–355

Mullen EK, Mccallum IS (2013) Coexisting pseudobrookite, ilmenite, and titanomagnetite in hornblende andesite of the Coleman Pinnacle flow, Mount Baker, Washington: evidence for a highly oxidized arc magma. Am Mineral 98(2–3):417–425

Mysen BO (1983) The structure of silicate melts. Annu Rev Earth Planet 11:75–97

Namur O, Charlier B, Toplis MJ, Higgins MD, Hounsell V, Liégeois JP, Vander AJ (2011) Differentiation of tholeiitic basalt to A-type granite in the Sept Iles layered intrusion. Canada J Petrol 52(3):487–539

Namur O, Charlier B, Holness MB (2012a) Dual origin of Fe–Ti–P gabbros by immiscibility and fractional crystallization of evolved tholeiitic basalts in the Sept Iles layered intrusion. Lithos 154:100–114. https://doi.org/10.1016/j.lithos.2012.06.034

Namur O, Charlier B, Toplis MJ, Vander Auwera J (2012b) Prediction of plagioclase-melt equilibria in anhydrous silicate melts at 1-atm. Contrib Mineral Petrol 163:133–150. https://doi.org/10.1007/s00410-011-0662-z

Naslund HR (1983) The effect of oxygen fugacity on liquid immiscibility in iron-bearing silicate melts. Am J Sci 283:1034–1059

Neave DA, Namur O (2022) Plagioclase archives of depleted melts in the oceanic crust. Geology 50(7):848–852

Neave DA, Putirka KD (2017) A new clinopyroxene-liquid barometer, and implications for magma storage pressures under Icelandic rift zones. Am Mineral 102(4):777–794

Neave DA, Namur O, Shorttle O, Holtz F (2019) Magmatic evolution biases basaltic records of mantle chemistry towards melts from recycled sources. Earth Planet Sci Lett 520:199–211

O'Neill HS (1987) Quartz-fayalite-iron and quartz–fayalite–magnetite equilibria and the free energy of formation of fayalite (Fe_2SiO_4) and magnetite (Fe_3O_4). Am Mineral 72(1–2):67–75

Pang K-N, Li C, Zhou M-F, Ripley EM (2008) Abundant Fe–Ti oxide inclusions in olivine from the Panzhihua and Hongge layered intrusions, SW China: evidence for early saturation of Fe–Ti oxides in ferrobasaltic magma. Contrib Mineral Petrol 156:307–321. https://doi.org/10.1007/s00410-008-0287-z

Pang K-N, Zhou M-F, Qi L, Shellnutt G, Wang CY, Zhao D (2010) Flood basalt-related Fe-Ti oxide deposits in the Emeishan large igneous province, SW China. Lithos 119(1–2):123–136. https://doi.org/10.1016/j.lithos.2010.06.003

Panjasawatwong Y, Danyushevsky LV, Crawford AJ, Harris KL (1995) An experimental study of the effects of melt composition on plagioclase-melt equilibria at 5 and 10 kbar: implications for the origin of magmatic high-An plagioclase. Contrib Mineral 118(4):420–432

Parman SW, Grove TL (2004) Harzburgite melting with and without H_2O: experimental data and predictive modeling. J Geophys Res. https://doi.org/10.1029/2003JB002566

Peate DW, Hawkesworth CJ, Mantovani MS (1992) Chemical stratigraphy of the Paraná lavas (South America): classification of magma types and their spatial distribution. Bull Volcanol 55:119–139

Philpotts AR (2008) Comments on: liquid immiscibility and the evolution of basaltic magma. J Petrol 49:2171–2175. https://doi.org/10.1093/petrology/egn061

Philpotts AR, Doyle CD (1983) Effect of magma oxidation state on the extent of silicate liquid immiscibility in a tholeiitic basalt. Am J Sci 283:967–986

Presnall DC, Dixon SA, Dixon JR, O'donnell TH, Brenner NL, Schrock RL, Dycus DW (1978) Liquidus phase relations on the join diopside-forsterite-anorthite from 1 atm to 20 kbar: their bearing on the generation and crystallization of basaltic magma. Contrib Mineral Petrol 66(2):203–220

Qi L, Wang CY, Zhou M-F (2008) Controls on the PGE distribution of Permian Emeishan alkaline and peralkaline volcanic rocks in Longzhoushan, Sichuan Province, SW China. Lithos 106:222–236. https://doi.org/10.1016/j.lithos.2008.07.012

Ren ZY, Wu YD, Zhang L, Nichols AR, Hong LB, Zhang YH, Zhang Y, Liu JQ, Xu YG (2017) Primary magmas and mantle sources of Emeishan basalts constrained from major element, trace element and Pb isotope compositions of olivine-hosted melt inclusions. Geochim Cosmochim Acta 208:63–85

Roeder PL, Emslie R (1970) Olivine-liquid equilibrium. Contrib Mineral Petrol 29(4):275–289

Rutherford MJ, Hess PC, Daniel GH (1974) Experimental liquid line of descent and liquid immiscibility for basalt 70017. Proc Lunar Planet Sci Conf 5:569–583

Ryerson FJ, Hess PC (1978) Implications of liquid–liquid distribution coefficients to mineral–liquid partitioning. Geochim Cosmochim Acta 42:921–932

Ryerson FJ, Hess PC (1980) The role of P_2O_5 in silicate melts. Geochim Cosmochim Acta 44(4):611–624

Snyder D, Carmichael IS, Wiebe RA (1993) Experimental study of liquid evolution in an Fe-rich, layered mafic intrusion: constraints of Fe–Ti oxide precipitation on the T-fO2 and T-ϱ paths of tholeiitic magmas. Contrib Mineral Petrol 113(1):73–86

Song XY, Zhou MF, Hou ZQ, Cao ZM, Wang YL, Li Y (2001) Geochemical constraints on the mantle source of the Upper Permian Emeishan continental flood basalts, Southwestern China. Int Geol Rev 43:213–225. https://doi.org/10.1080/00206810109465009

Song X-Y, Qi H-W, Hu R-Z, Chen L-M, Yu S-Y, Zhang J-F (2013) Formation of thick stratiform Fe–Ti oxide layers in layered intrusion and frequent replenishment of fractionated mafic magma: evidence from the Panzhihua intrusion, SW China. Geochem Geophys 14(3):712–732. https://doi.org/10.1002/ggge.20068

Tao Y, Putirka K, Hu R-Z, Li C (2015) The magma plumbing system of the Emeishan large igneous province and its role in basaltic magma differentiation in a continental setting. Am Mineral 100:2509–2517

Tegner C, Cawthorn RG, Kruger FJ (2006) Cyclicity in the main and upper zones of the Bushveld Complex, South Africa: crystallization from a zoned magma sheet. J Petrol 47(11):2257–2279

Toplis MJ (2005) The thermodynamics of iron and magnesium partitioning between olivine and liquid: criteria for assessing and predicting equilibrium in natural and experimental systems. Contrib Mineral Petrol 149(1):22–39

Toplis MJ, Carroll MR (1995) An Experimental study of the influence of oxygen fugacity on Fe–Ti oxide stability, phase relations, and mineral-melt equilibria in ferro-basaltic systems. J Petrol 36:1137–1170. https://doi.org/10.1093/petrology/36.5.1137

Toplis MJ, Libourel G, Carroll MR (1994) The role of phosphorus in crystallisation processes of basalt: an experimental study. Geochim Cosmochim Acta 58(2):797–810

Tormey DR, Grove TL, Bryan WB (1987) Experimental petrology of normal MORB near the Kane Fracture Zone: 22–25 N, mid-Atlantic ridge. Contrib Mineral Petrol 96(2):121–139

VanTongeren JA, Mathez EA (2012) Large-scale liquid immiscibility at the top of the Bushveld complex, South Africa. Geology 40(6):491–494. https://doi.org/10.1130/g32980.1

Veksler IV (2009) Extreme iron enrichment and liquid immiscibility in mafic intrusions: experimental evidence revisited. Lithos 111(1–2):72–82

Veksler IV, Charlier B (2015) Silicate liquid immiscibility in layered intrusions. Layered intrusions. Springer, Berlin, pp 229–258

Villiger S, Ulmer P, Müntener O, Thompson AB (2004) The liquid line of descent of anhydrous, mantle-derived, tholeiitic liquids by fractional and equilibrium crystallization—an experimental study at 1.0 GPa. J Petrol 45:2369–2388

Villiger S, Ulmer P, Müntener O (2007) Equilibrium and fractional crystallization experiments at 0.7 GPa; the effect of pressure on phase relations and liquid compositions of tholeiitic magmas. J Petrol 48:159–184

Voigt M, Coogan LA, von der Handt A (2017) Experimental investigation of the stability of clinopyroxene in mid-ocean ridge basalts: the role of Cr and Ca/Al. Lithos 274:240–253

Wang CY, Zhou M-F, Qi L (2007) Permian flood basalts and mafic intrusions in the Jinping (SW China)–Song Da (northern Vietnam) district: mantle sources, crustal contamination and sulfide segregation. Chem Geol 3:317–343

Wang K, Wang CY, Ren Z-Y (2018) Apatite-hosted melt inclusions from the Panzhihua gabbroic-layered intrusion associated with a giant Fe–Ti oxide deposit in SW China: insights for magma unmixing within a crystal mush. Contrib Mineral Petrol 173:59. https://doi.org/10.1007/s00410-018-1484-z

Wang K, Dong H, Ou Q, Liu R (2021) Large-scale liquid immiscibility in the Hongge layered intrusion hosting a giant Fe–Ti oxide deposit in SW China. Ore Geol Rev 136:104268

Xiao L, Xu YG, Mei HJ, Zheng YF, He B, Pirajno F (2004) Distinct mantle sources of low-Ti and high-Ti basalts from the western Emeishan large igneous province, SW China: implications for plume–lithosphere interaction. Earth Planet Sci Lett 228:525–546. https://doi.org/10.1016/j.epsl.2004.10.002

Xiong F, Tao Y, Liao M, Liao Y, Ma J (2021) Liquid immiscibility in the Panzhihua intrusion, SW China: evidence from ore textures and Fe–Ti oxide-rich globules in gabbros. J Asian Earth Sci 209:104683. https://doi.org/10.1016/j.jseaes.2021.104683

Xu Y, Chung S-L, Jahn B, Wu G (2001) Petrologic and geochemical constraints on the petrogenesis of Permian-Triassic Emeishan flood basalts in southwestern China. Lithos 58:145–168. https://doi.org/10.1016/S0024-4937(01)00055-X

Xu Y, Mei H, Xu J et al (2003) Origin of two differentiation trends in the Emeishan flood basalts. Chin Sci Bull 48:390–394. https://doi.org/10.1007/BF03183236

Xu R, Li Y, Lambart S (2020) Melting of a hydrous peridotite mantle source under the Emeishan large igneous province. Earth Sci Rev 207:103253

Yuan Q, Namur O, Fischer LA, Roberts RJ, Lü X, Charlier B (2017) Pulses of plagioclase-laden magmas and stratigraphic evolution in the Upper Zone of the Bushveld complex, South Africa. J Petrol 58(8):1619–1643. https://doi.org/10.1093/petrology/egx067

Zhang Z, Mahoney JJ, Mao J, Wang F (2006) Geochemistry of picritic and associated basalt flows of the western Emeishan flood basalt province, China. J Petrol 47:1997–2019

Zhang D, Zhang Z, Huang H, Cheng Z, Charlier B (2018) Petrogenesis and metallogenesis of the Wajilitag and Puchang Fe–Ti oxide-rich intrusive complexes, northwestern Tarim Large Igneous Province. Lithos 304–307:412–435. https://doi.org/10.1016/j.lithos.2018.02.019

Zhou MF, Robinson PT, Lesher CM, Keays RR, Zhang CJ, Malpas J (2005) Geochemistry, petrogenesis and metallogenesis of the Panzhihua Gabbroic layered intrusion and associated Fe–Ti–V oxide deposits, Sichuan Province, SW China. J Petrol 46:2253–2280. https://doi.org/10.1093/petrology/egi054

Zhou MF, Arndt NT, Malpas J, Wang CY, Kennedy AK (2008) Two magma series and associated ore deposit types in the Permian Emeishan large igneous province, SW China. Lithos 103:352–368. https://doi.org/10.1016/j.lithos.2007.10.006

Zhou M, Chen WT, Wang CY, Prevec SA, Liu P, Howarth GH (2013) Two stages of immiscible liquid separation in the formation of Panzhihua-type Fe–Ti–V oxide deposits, SW China. Geosci Front 4:481–502. https://doi.org/10.1016/j.gsf.2013.04.006

Journal:	**410**
Article:	**1990**

Author Query Form

Please ensure you fill out your response to the queries raised below and return this form along with your corrections

Dear Author

During the process of typesetting your article, the following queries have arisen. Please check your typeset proof carefully against the queries listed below and mark the necessary changes either directly on the proof/online grid or in the 'Author's response' area provided below

Query	Details Required	Author's Response
AQ1	Please confirm the section headings are correctly identified.	